Electronic Supplementary Material (ESI) for Energy & Environmental Science.

Supporting Information

Neutron and X-Ray Tomography at NeXT

Measurement Setup

The 3D distribution of lithium within the cells can be studied using neutron computed tomography (NCT), and was performed at an unprecedented spatial resolution at a pixel size of 4.2 µm. The experiment was done on the NeXT instrument at the ILL(1), which provides a cold neutron beam from a reactor source (see Methods). On this instrument, an additional 150 kV X-ray tube with a tungsten target is also available to provide a divergent X-ray cone beam, which enables both neutron- and X-ray tomography without dismounting the cell. Both NCT and XCT result in 3D-volumes of the cells after reconstruction due to the full-field nature of these imaging methods (see S1 – S5).

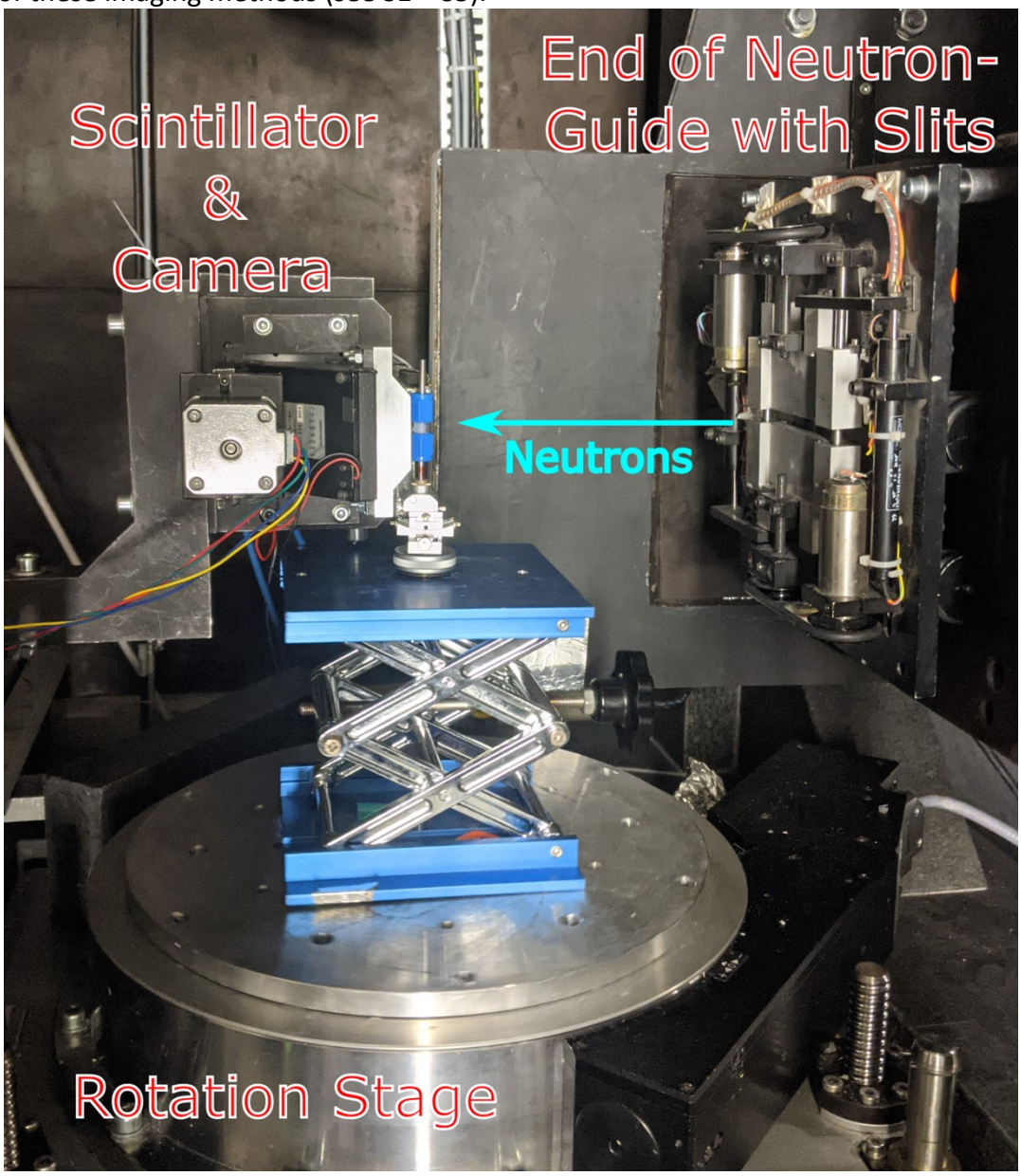

Figure S1: Picture of the measurement setup used for the neutron tomography at NeXT of ILL. The sample pictured is a different cell type but employs an identical setup as the experiment described in the text.

Image Analysis

The processing of the raw neutron tomography data and reconstruction was performed using the Ufo(2) and Tofu(3) libraries. The first step consists of flat field correcting the raw projections (Figure S1) using flat and dark images acquired during the measurements. These corrected images (Figure S2) are then used in the reconstruction process and the raw volume is sliced horizontally to obtain 2D images, with an example shown in Figure S3. Finally, the post processing consists of running a rolling median filter over 15 slices at a time to reduce noise, resulting in the processed image in Figure S4.

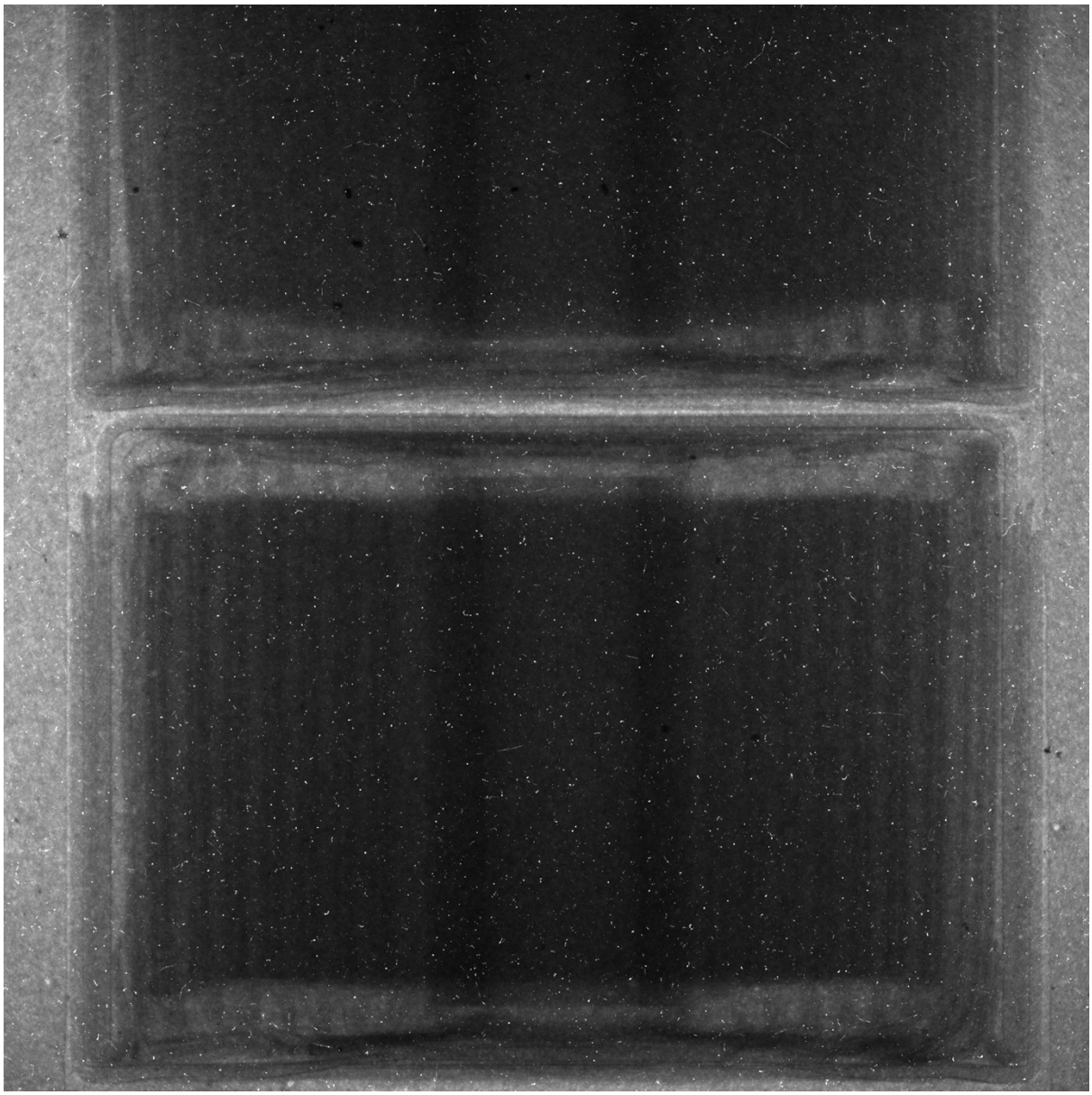

Figure S2: Raw Neutron Projection image before any preprocessing steps. Sized 2048x2048 pixels. Contrast adjusted to 190 – 2704 a.u. for visibility.

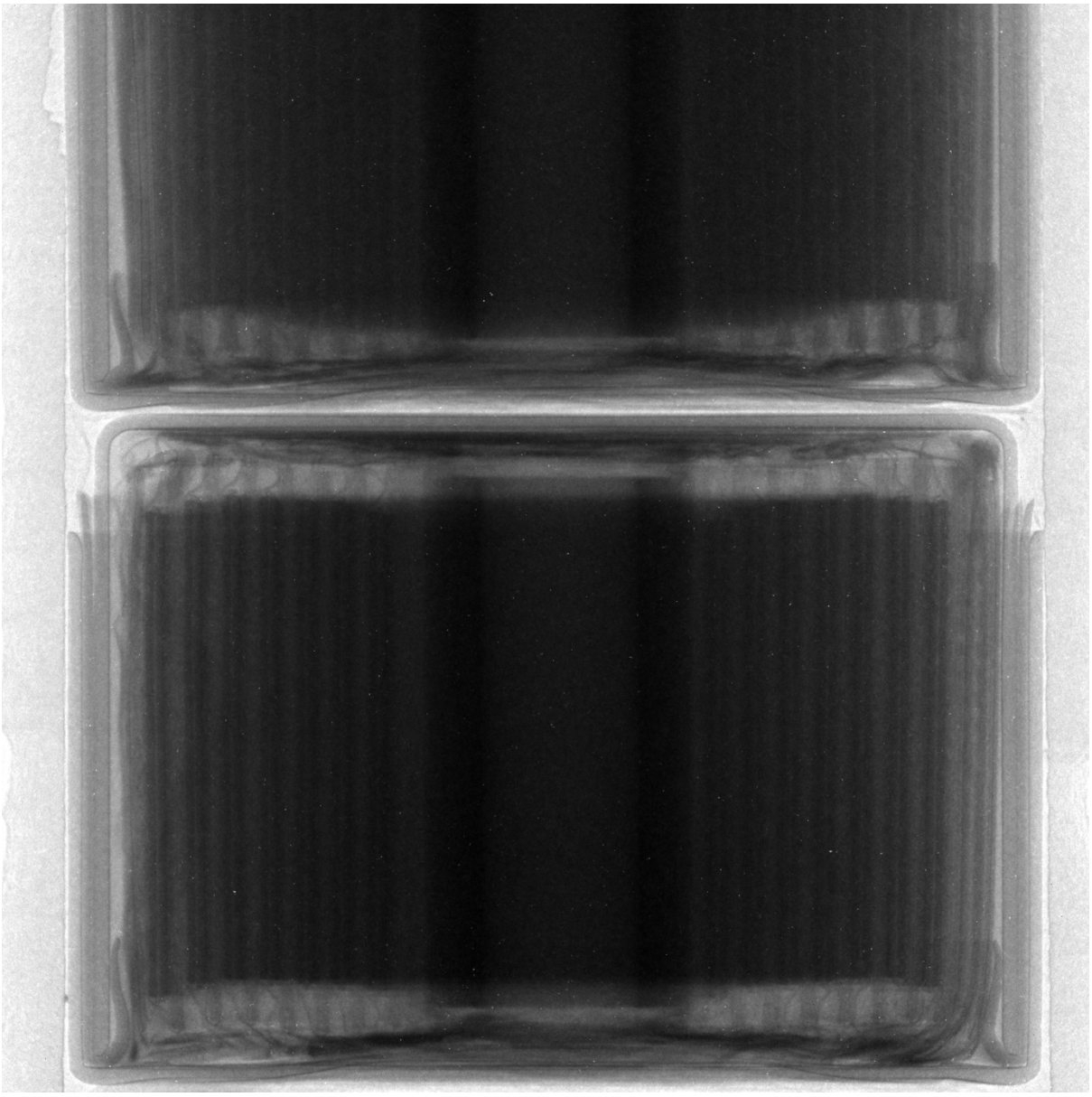

Figure S3: Flat-Field corrected Neutron Radiography sample. Three projections were averaged using a rolling-average window to remove most of the white-spots caused by high energy gamma-rays. Contrast adjusted to 12.38 – 100 % Transmission.

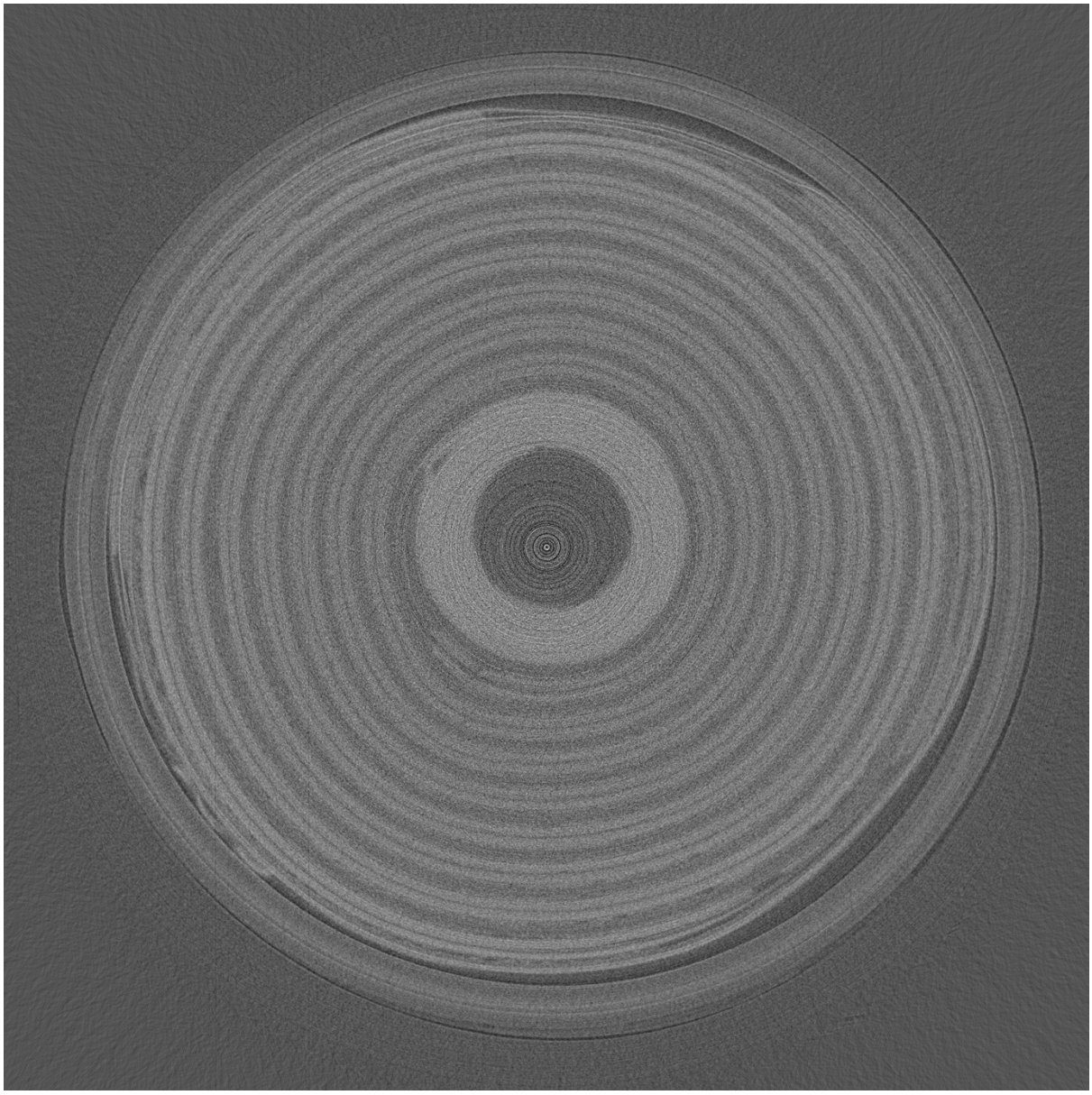

Figure S4: 2D horizontal slice through the raw reconstructed neutron tomography volume before any post processing steps.

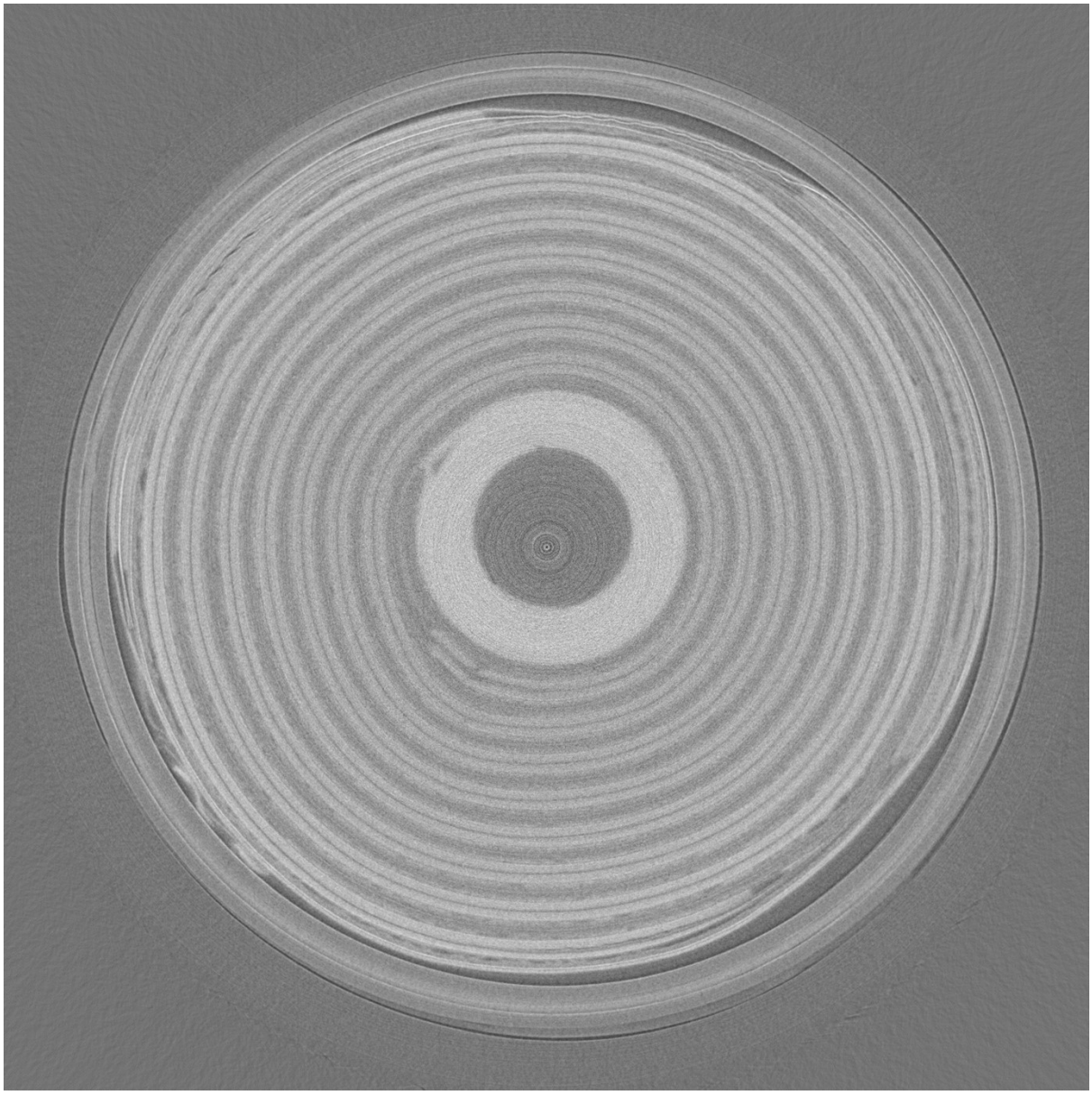

Figure S5: 2D horizontal slice through the processed neutron tomography volume after applying a rolling median with a window of 15 slices

X-Ray Tomography

The X-ray computed tomography (XCT) data is very useful in the segmentation of the components by correlating the attenuation data from the two probes. The reconstruction was performed with the software X-Act provided by the device manufacturer RX Solutions with exemplary data shown in Figures S6 and S7.

Figure S6: Raw X-ray projection image before reconstruction. Sized 1712x2096 pixels. Contrast adjusted to 2760 – 23997 a.u. for visibility.

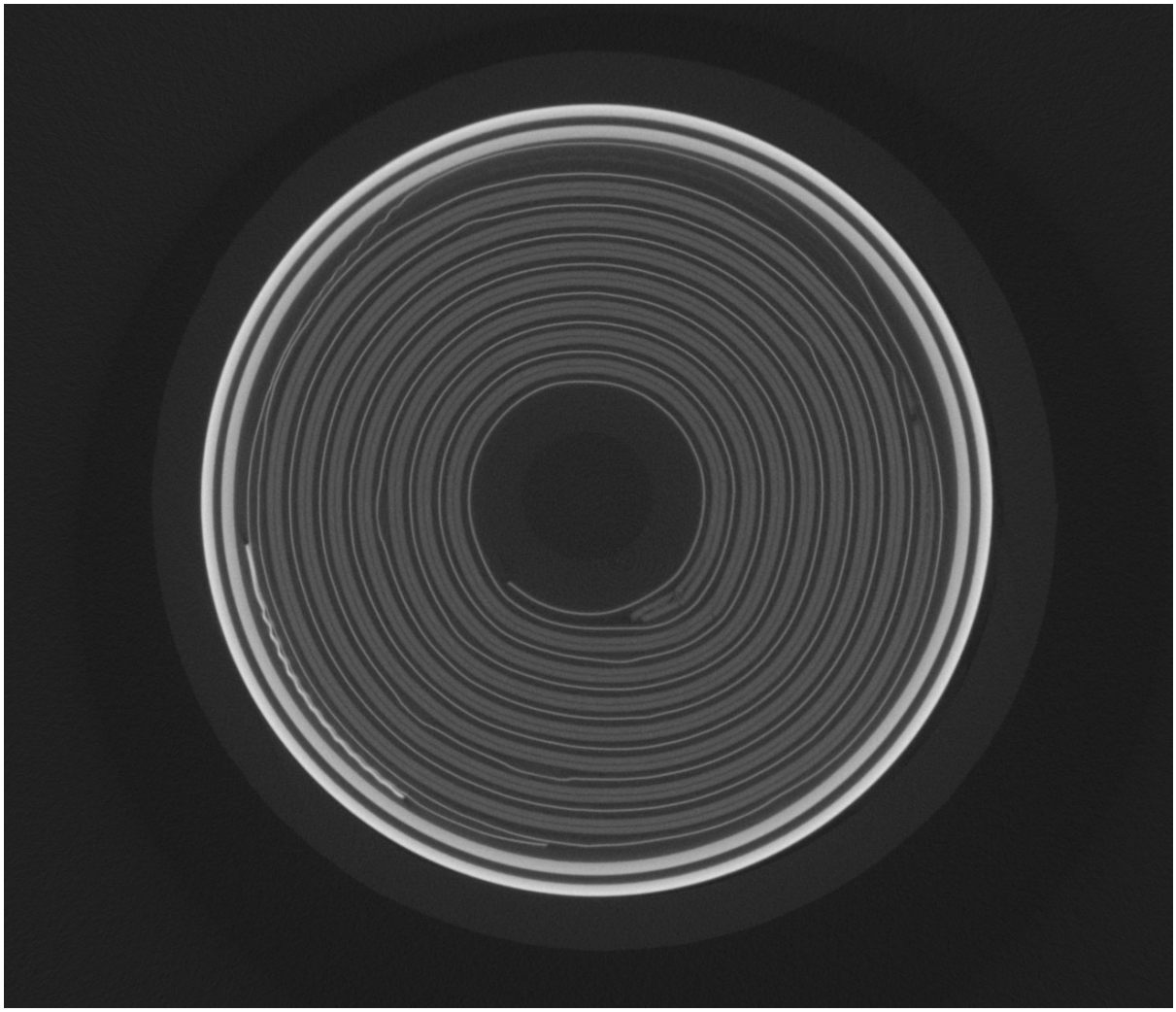

Figure S7: 2D horizontal slice through the raw reconstructed X-ray tomography volume as exported from the software.

Combined Neutron and X-Ray Tomography

To combine both modalities into a single volume they must be aligned. This is done by scaling the images to match in size and then running multimodal registration as described in (4) and implemented in (5). This results in a deformation tensor, which is then applied to the neutron data to produce the aligned data. Finally, the volumes are combined in false color by encoding the X-Ray data as the red color channel and the neutron data as both green and blue, producing a cyan color in the images. A slice of this combination is depicted in Figure S8.

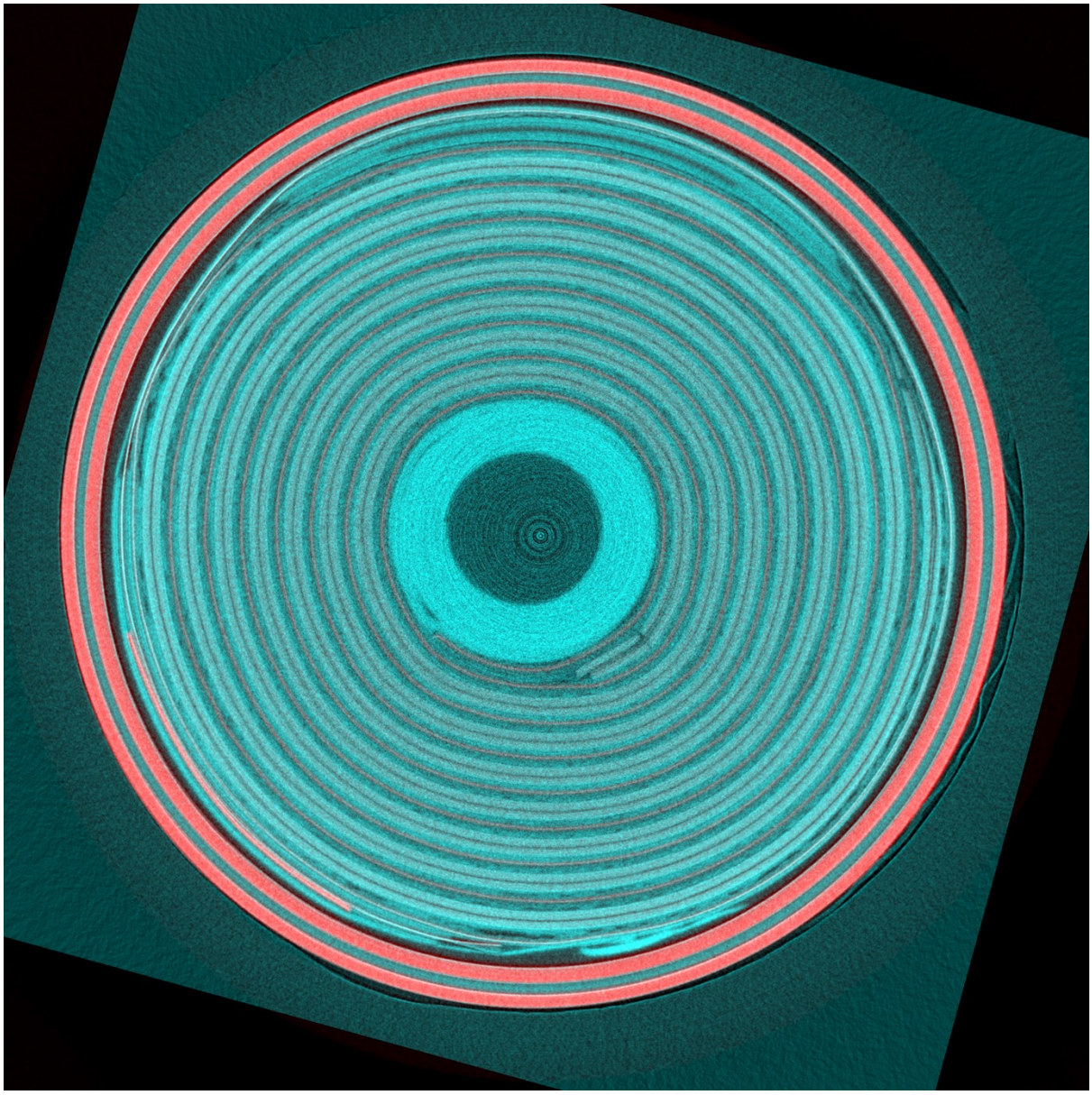

Figure S8: 2D slice of the aligned and combined NXCT volumes before contrast adjustments. The neutron volume was deformed with the deformation determined with multimodal registration to match the X-ray volume.

Interpretation Details

The rolled geometry of the cells is clearly visible from these images. Zooming into the cell geometry (insert in the main text, Figure 1e) enables the comparison of the XCT data with NCT data in more detail, making the complementary nature of these modalities clear. Some components, like the NMC cathodes, coated on both sides of the aluminum current collector, are both neutron and X-ray attenuating due to their high cobalt/nickel content and, therefore, are well contrasted in both modalities. They appear as a broad double stripe, with the Al foil distinguishable in the center. Other components, like the stainless-steel cell casing, are well contrasted in one modality (XCT) and still recognizable in the other one (NCT), but less intensely. Most interestingly, some components are only visible in one of the modalities. For instance, the plastic center roll of the cell is detected in the neutron scans due to the strong interaction with hydrogen contained in the polymer, but is almost invisible with X-rays. On the contrary, the thin ribbon of the anode-side copper current collector can be precisely

located by XCT but is almost unresolved with neutrons. In general, one can notice that the XCT image is much more defined, while the NCT looks more blotchy, particularly with the copper current collector only faintly visible in the middle of the anode, where various bright and dark spots are distributed. This is not a resolution limitation or an artefact, but can rather be attributed to lithium sensitive neutron absorption and lithium-insensitive X-ray absorption, which is unable to distinguish lithium accumulated or depleted regions from the attenuation value. In the neutron image however, attenuation variations in the interior of the cell must arise mostly from lithium content variations because of the pronounced difference in neutron cross section for lithium (71.87 barn(6)) with respect to all other elements present in the cell besides hydrogen (e.g. 82.35 barn for H, 5.55 barn for C, 2.34 barn for Si, or 42.78 barn for Co(6)) . Therefore, the blotchy microstructure observed in NCT indicates the uneven lithium repartition in the aged cell. This becomes even more pronounced when comparing the aged cell with a reference cell without an electrolyte and therefore no ageing or lithium repartition effects, as in Figure S9.

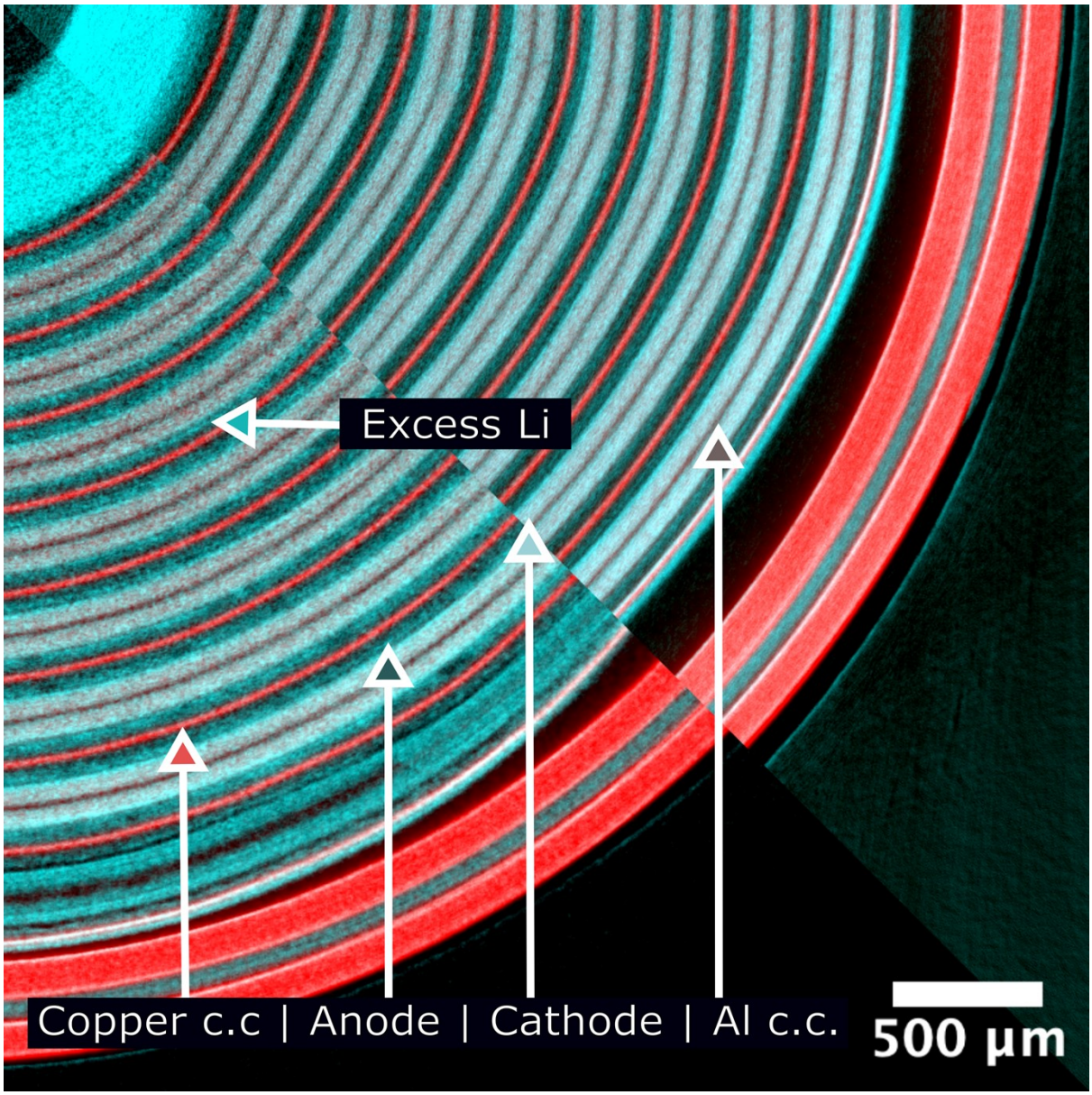

Figure S9: Direct comparison of NXCT data for the aged cell in the discharged state, with a reference cell not including any electrolyte. Components inside the cell are labelled, as well as lithium remaining in the anode being highlighted.

Small- and Wide-Angle X-ray Scattering Computed Tomography at ID31

Measurement Setup

While NXCT imaging of the cells gives evidence on the local lithium concentration, there is no structural information in this data. It ignores in which state the lithium is, and in which phase it is localized. This gap is filled by acquiring 2D-resolved structural patterns, which provide the missing information on material phases and properties. The same fresh and aged cells were measured on the ID31 beamline at ESRF. By adjusting the distance between the sample and detector, wide-angle and small-angle scans were acquired successively (Main Text, Figure 1c), resolving both atomic scale and nanoscale structures, respectively. SAXS-CT and WAXS-CT data acquisition and analysis is described in Methods and Figures S10 – S11, and the processing of typical data is shown in Figures S12 – S16. The XRD patterns captured in the

WAXS-CT scans contain peaks from the crystallographic components of the cell, with particular interest on (de)lithiated NMC and (de)lithiated graphite (e.g. Li_xC_6). 2D phase mapping of the WAXS data is performed by rendering a selected Bragg peak integral in each pixel (C_6, Bragg reflection 003, q = 1.82 – 1.90 $Å^{-1}$, for main Figure 1d, left panel). This allows one to selectively visualize any crystalline component, as shown for the graphite in the anode as an example in main Figure 1d. Other components are shown in Figures S17 – S21. Moreover, the SAXS data can also be treated to provide additional 2D maps. In this case, the scattered signal mostly arises from the nanosized silicon phase. Variations of the scattering profiles in intensity and shape can be analyzed to account for compositional and morphological changes due to lithiation. For example, main Figure 1d right panel shows the integral of the SAXS data between q = 0.025 – 0.1 $Å^{-1}$, which is mostly influenced by expanded silicon(7) (e.g., Li_xSi). Altogether, the WAXS-CT and SAXS-CT slice reconstructions shown in main Figure 1d both display the location of the composite anode. However, the WAXS map shows graphite in a given state of lithiation while the SAXS map shows silicon according to the expansion state. Hence, phase decoupling and identification is performed by Q-screening the scattering data, giving simultaneous non-destructive access to the structure and lithiation state of all active components in the same cell location.

Since all techniques were performed on the same cell, the scans can be matched and correlated with each other. Main Figure 1e shows the rendered 3D volume obtained with NXCT digitally cut in half, with the SWAXS data displayed in the height of the cell where it was measured. This position was determined as outlined in Methods. The top part of the 3D cell shows the raw XCT, the middle the raw NCT and the bottom the combined NXCT data, with X-ray attenuation displayed in red and neutron attenuation displayed in cyan. The inlet highlights observed cell damage with labeled components, which is discussed further in the text.

Figure S10 shows the measurement setup employed for the wide-angle X-Ray scattering measurements, while Figure S11 shows the alternative small angle X-ray scattering setup. The switch between the two modes was performed automatically using various motors to move the detector as far away from the sample as possible (roughly 6m) and inserting a fly tube under vacuum to limit the air scattering signal.

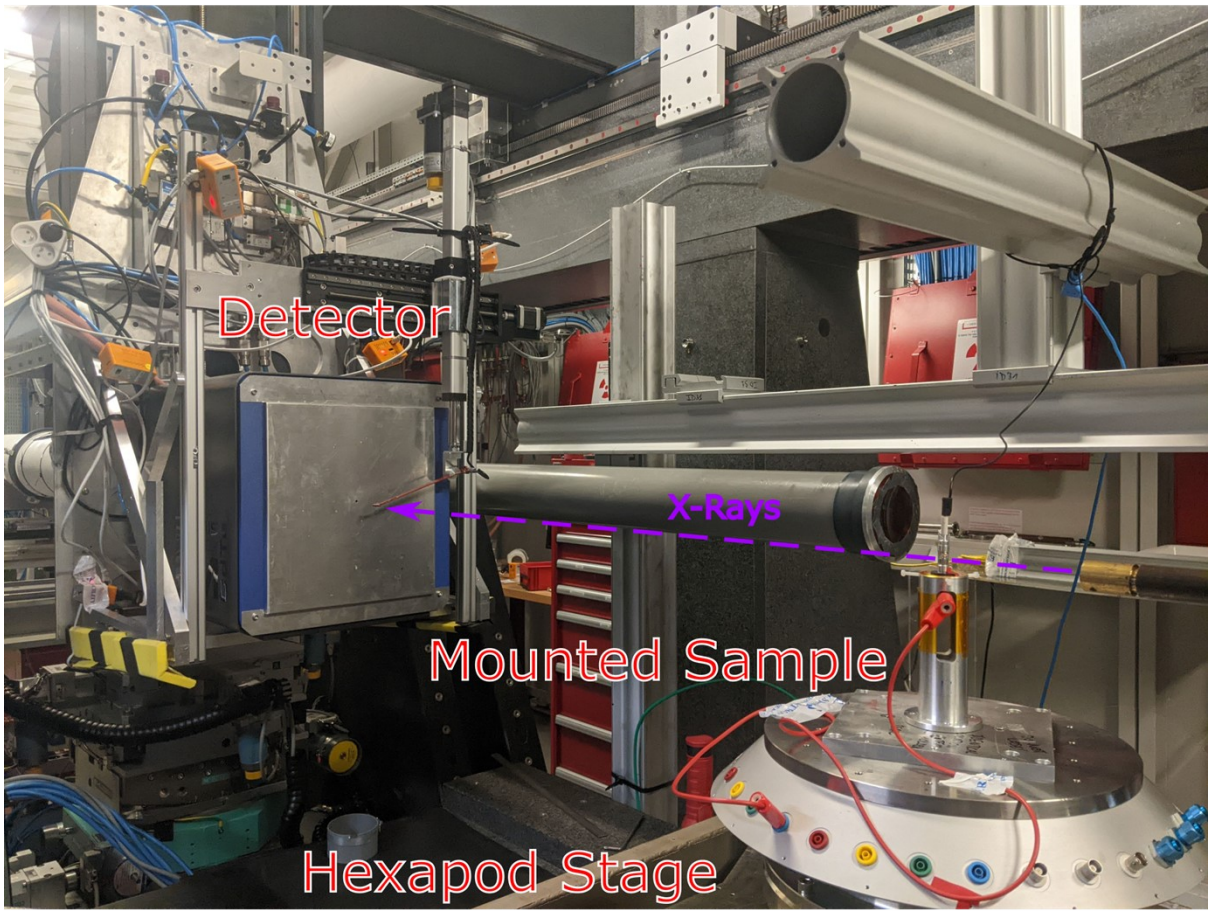

Figure S10: Picture of the measurement setup for wide angle X-ray scattering employed at ID31 of ESRF, with the sample mounted on the hexapod stage, which includes motors for rotation, translation as well as tilting to align the cell. The electrical connection to the potentiostat was done with cables, as well as a slipring to enable rotation.

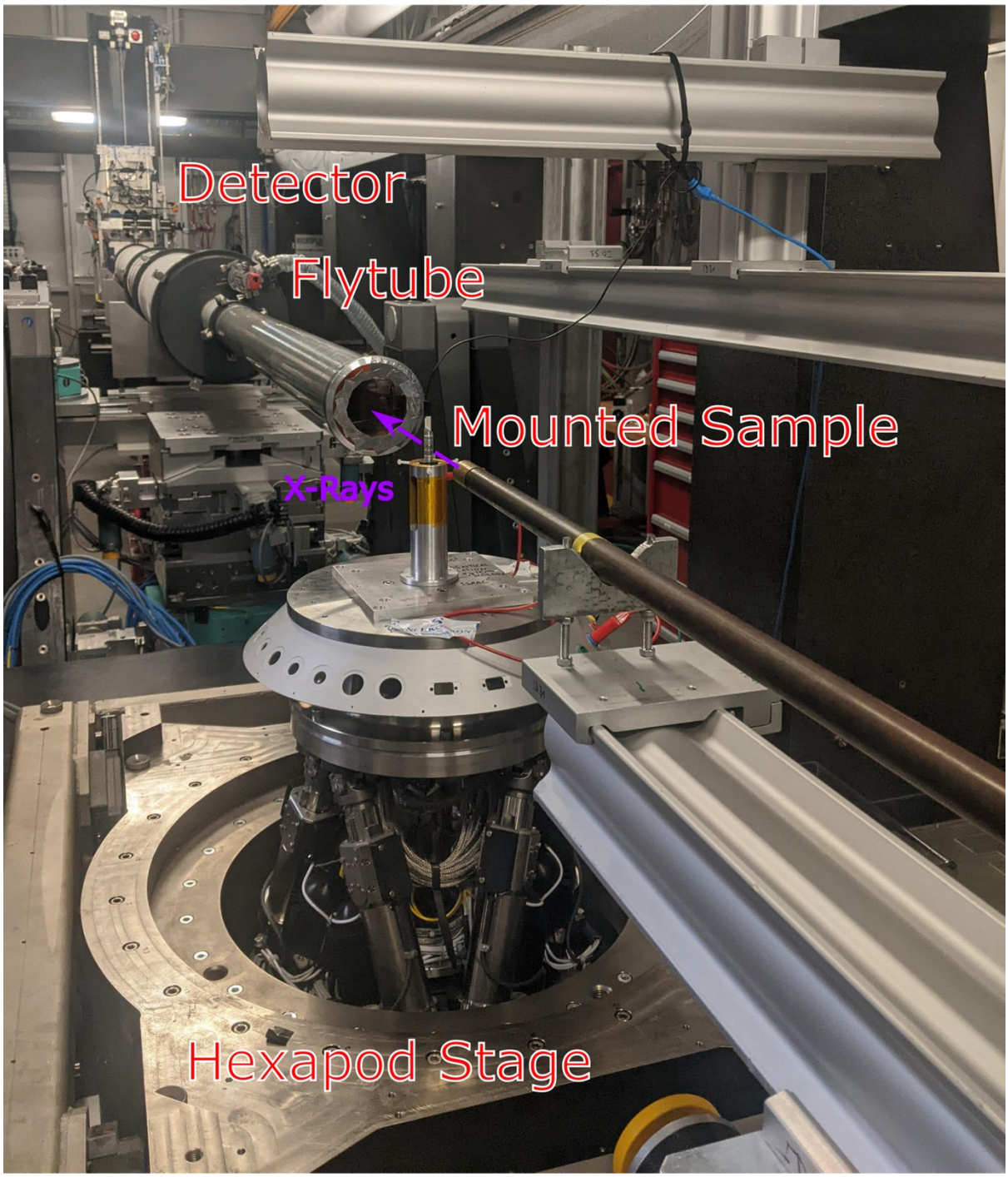

Figure S11: Picture of the measurement setup for wide angle X-ray scattering employed at ID31 of ESRF. The 6 m fly tube was inserted to limit air-scattering.

Processing

The image analysis of the Small and Wide Angle X-ray Scattering Computed Tomography (SWAXS-CT) was done using pyFAI(8) to radially integrate the 2D detector images and the astra-toolbox(9,10) to perform the reconstruction. Figure S12 shows a raw 2D detector image acquired with a Pilatus3 X CdTe 2M detector in the WAXS setup, with the azimuthally integrated diffraction pattern in Figure S13. Figure S14 shows the raw 2D detector image acquired with the same detector in the SAXS setup, with the azimuthally integrated data in Figure S15. After integration the data is arranged into sinograms, with an example in Figure S16. The sinograms were then centered by comparing the 0° and 180° scans to determine the

rotation axis, normalized and the air signal subtracted in the WAXS-CT scans, followed by the reconstruction. For the SAXS-CT data a transmission correction was done instead of the normalization and air subtraction. The reconstructed data can then be analyzed by Q-screening for regions of interest, as shown in figures S17 to S21.

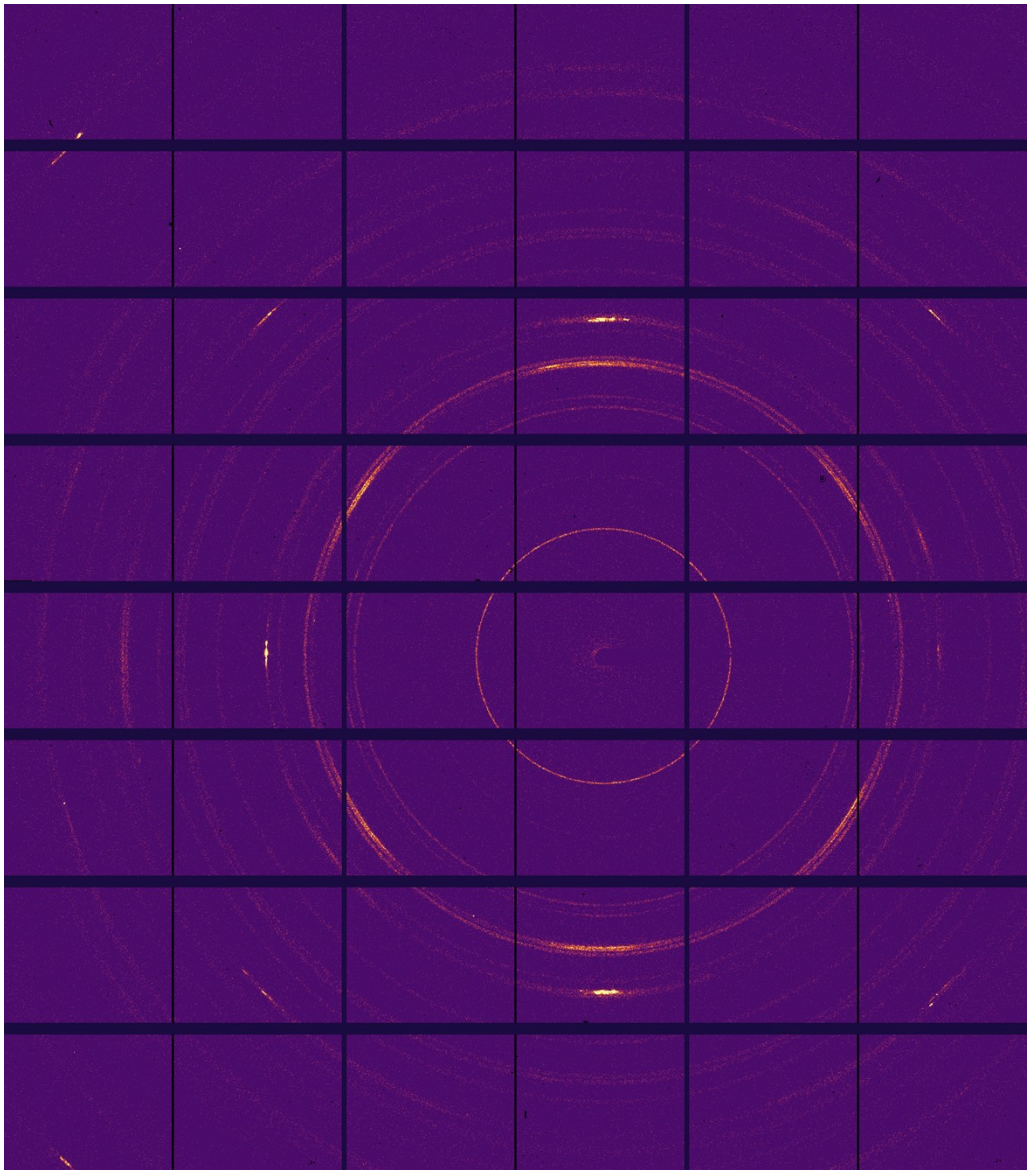

Figure S12: 2D detector image sample in WAXS position. Scaled -2 to 8 for visibility.

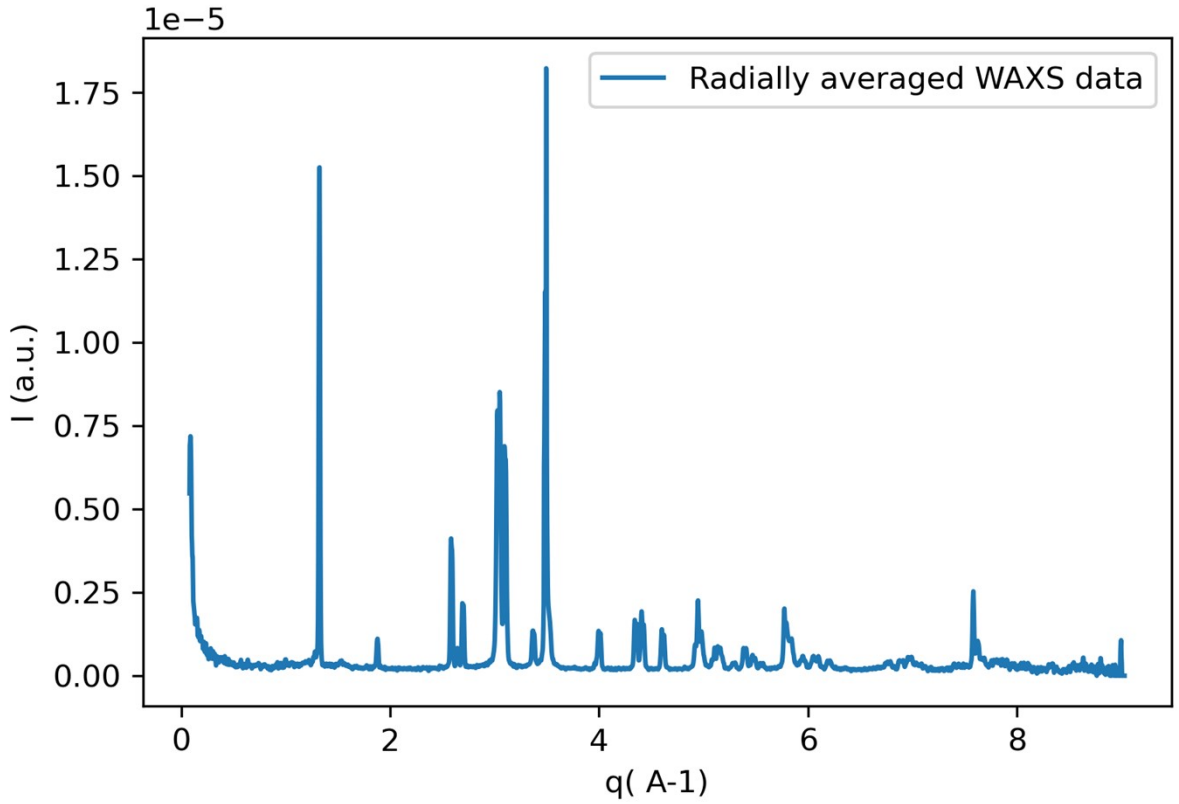

Figure S13: Radially integrated 2D WAXS data sample.

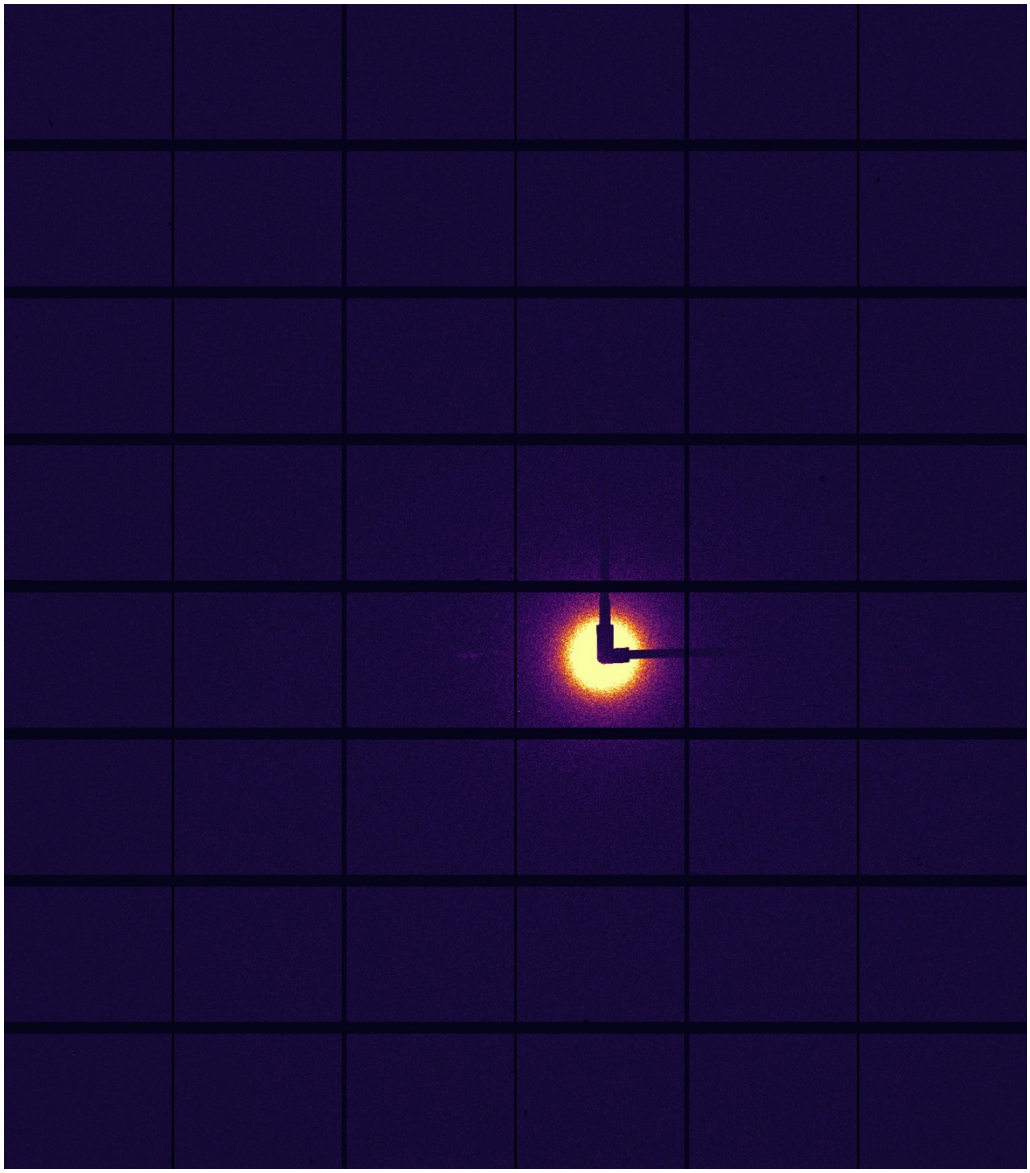

Figure S14: 2D detector image sample in SAXS position. Scaled -2 to 20 for visibility.

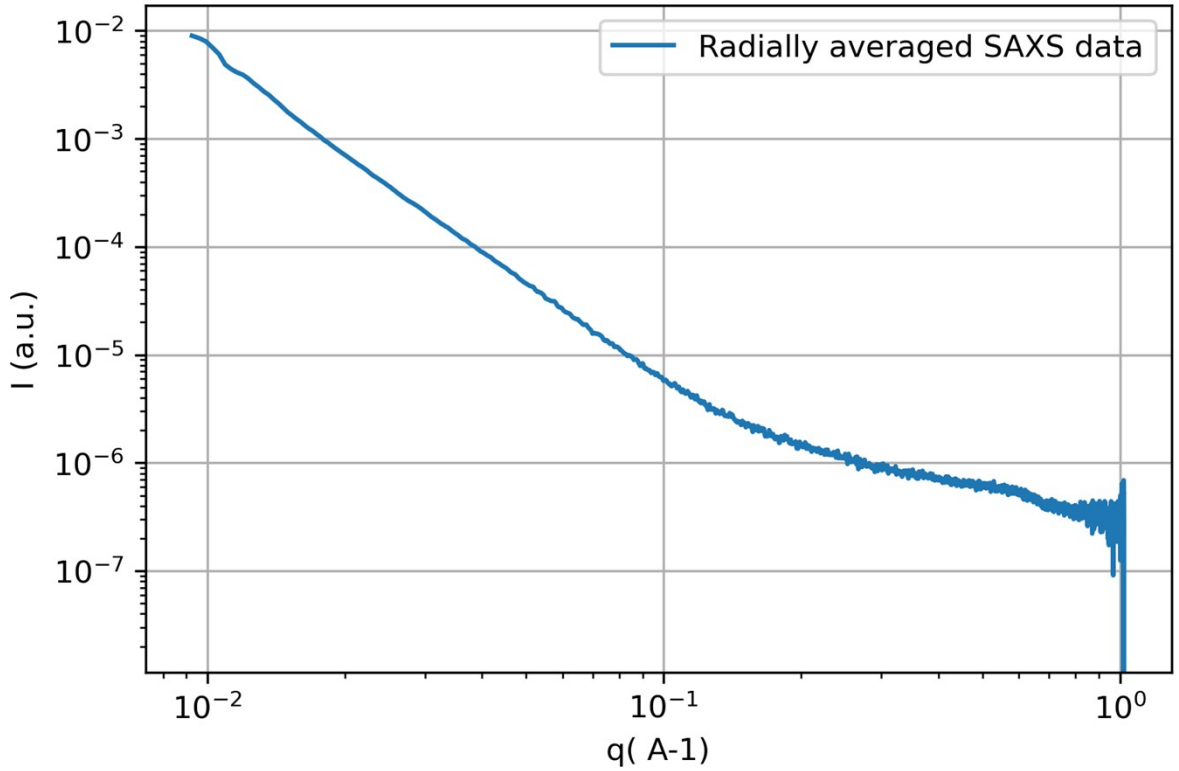

Figure S15: Archetypal 1D SAXS profile obtained from radially-integrating the 2D SAXS pattern, represented in a log-log diagram vs the momentum transfer q.

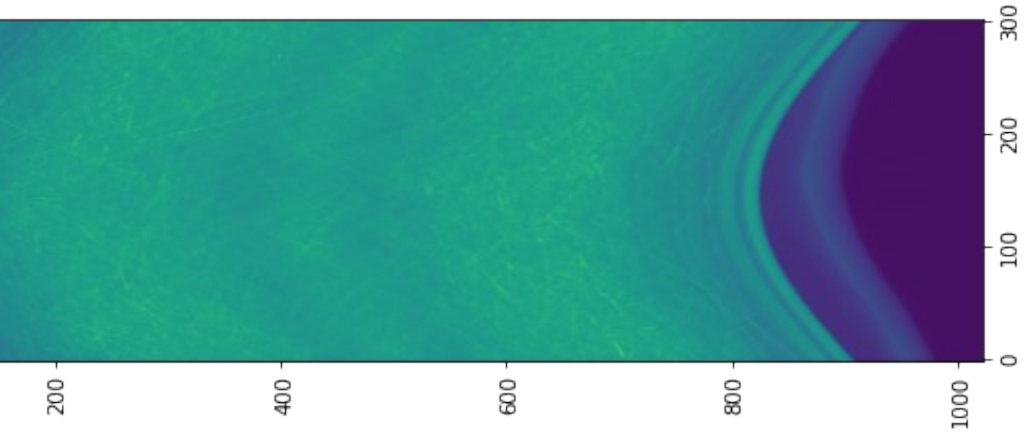

Figure S16: Exemplary Sinogram used to reconstruct the data. Each pixel represents the sum of a 1D WAXS pattern (as shown in S12) to better display the data. In practice there is a sinogram for every point in q-space, which is reconstructed separately.

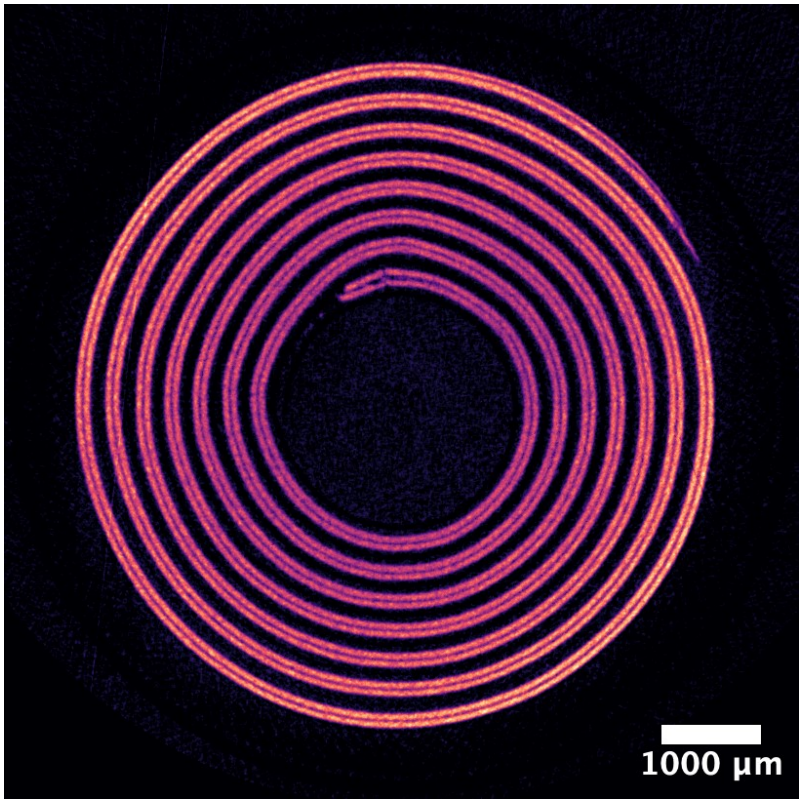

Figure S17: Integrated WAXS-CT intensity for lithiated NMC622 in the discharged aged cell, q = 4.57 – 4.62 Å^{-1}

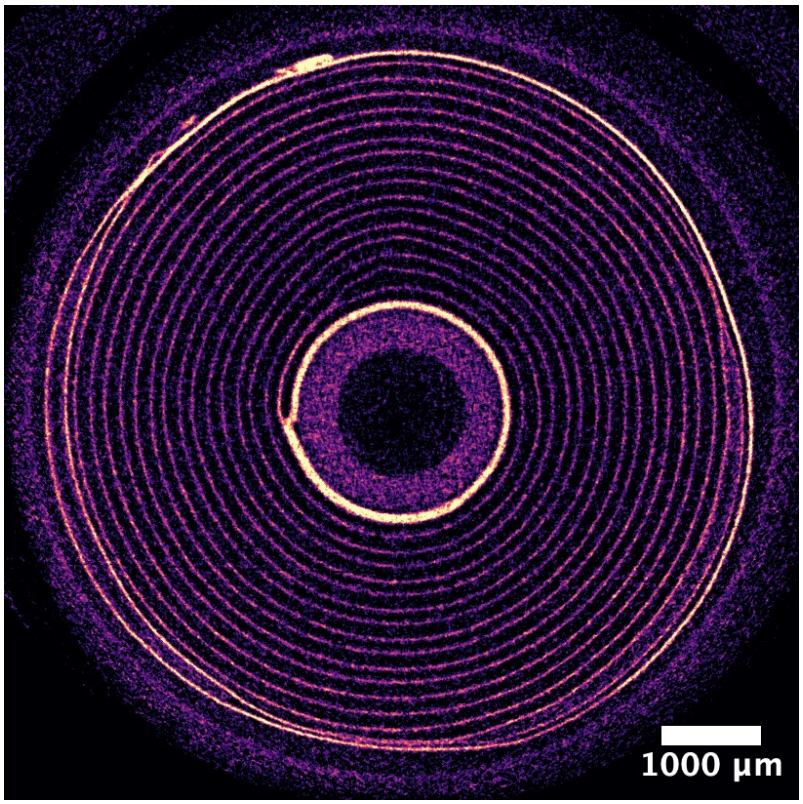

Figure S18: Integrated WAXS-CT intensity related to the separator and other polymer based components in the discharged aged cell, q = 1.50 – 1.56 Å^{-1}

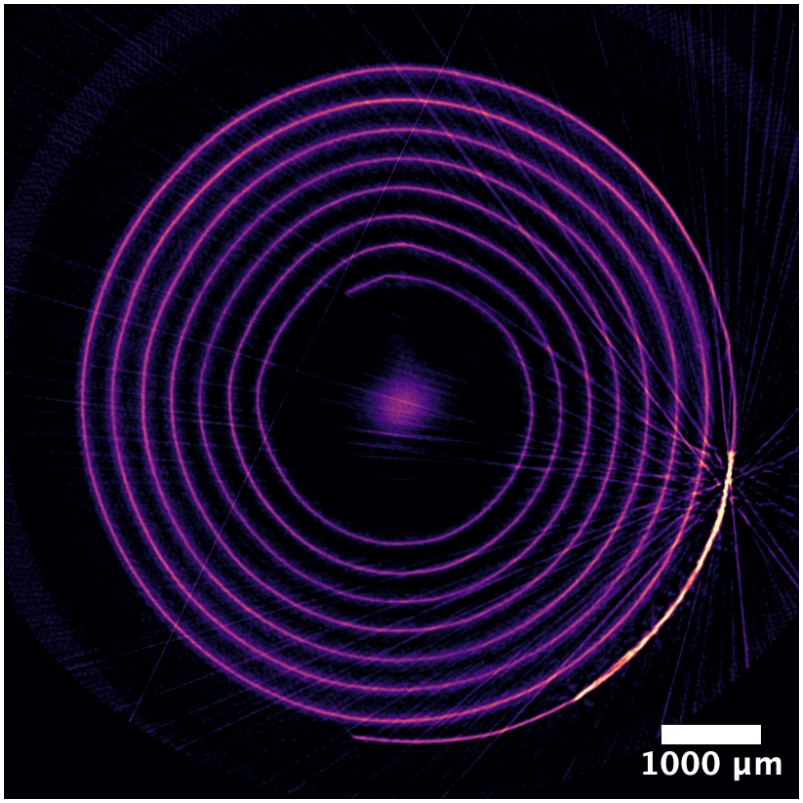

Figure S19: Integrated WAXS-CT intensity for aluminum in the discharged aged cell, mostly related to the cathode current collector and related current collector tab. Streaking can be observed originating from the welded current collector tab, which implies textured crystallites in that area. q = 2.66 – 2.72 Å^{-1}

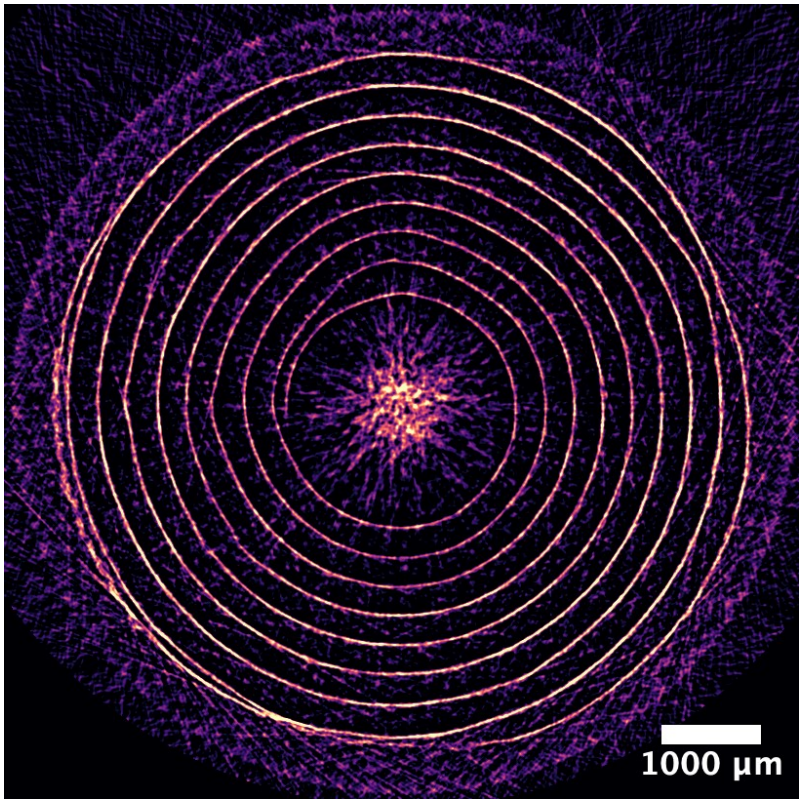

Figure S20: Integrated WAXS-CT intensity for copper in the discharged aged cell, mostly related to the anode current collector and related current collector tab. Heavy streaking can be observed, which shows heavy texture being present in the rolled copper foil used for the anode. q = 4.85 – 4.95 Å^{-1}

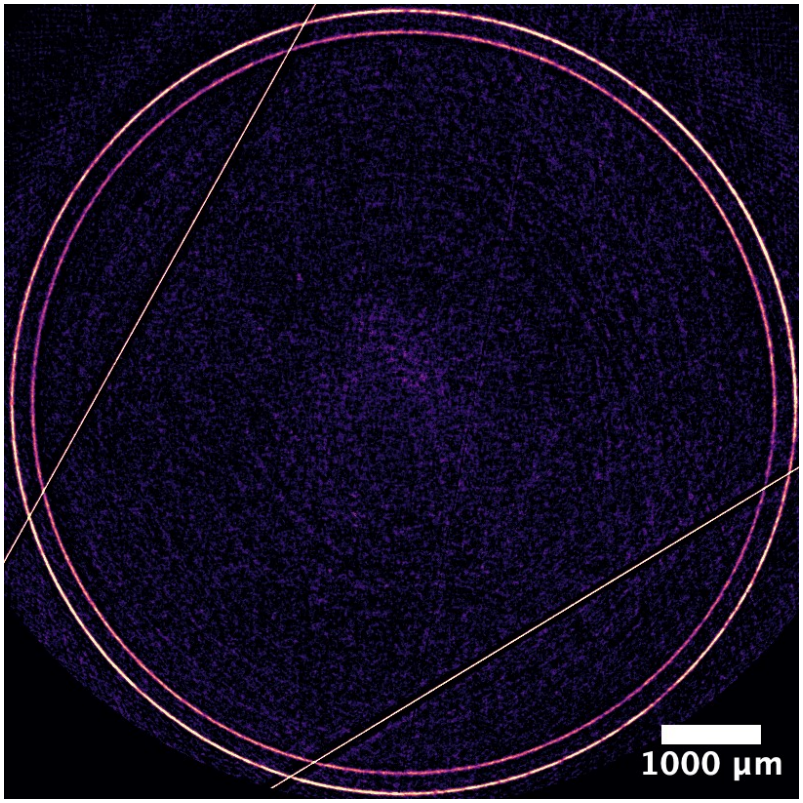

Figure S21: Integrated WAXS-CT intensity related to some component in the casing. Random streaks can be observed probably originating from large grains. Used to find the center of the cell for the virtual unrolling. q = 5.05 – 5.08 Å^{-1}

Localizing and Exploring Cell damage in the Fresh Cell

After virtual unrolling, we are in a better position to directly identify the changes occurring to the different components after charging the cell, as we can compare the images side by side. By combining the raw images obtained from the different modalities and displaying them in false color it becomes possible to directly compare the changes between states of charge as well as states of health. Fig 2a shows the aged cell and Fig S22 shows the equivalent evaluation for the fresh cell. Panels a) to d) represent the different modalities. All images show the same position in the same cell, which then further allows one to match the features visible in the different modalities. This depiction allows access to lithium concentration (Figure S22a and Main fig. 2a, correlated NXCT data), NMC state (Figure S22b and Fig. 2b, WAXS-CT), graphite state (Figure S22c and Fig. 2c, WAXS-CT) and silicon state (Figure S22d and Fig. 2d, SAXS-CT). Additionally, Figure S23 shows a zoom onto separate electrode windings for both an aged and a fresh cell when measured with NXCT. Gaps in the lithiation in both states are highlighted.

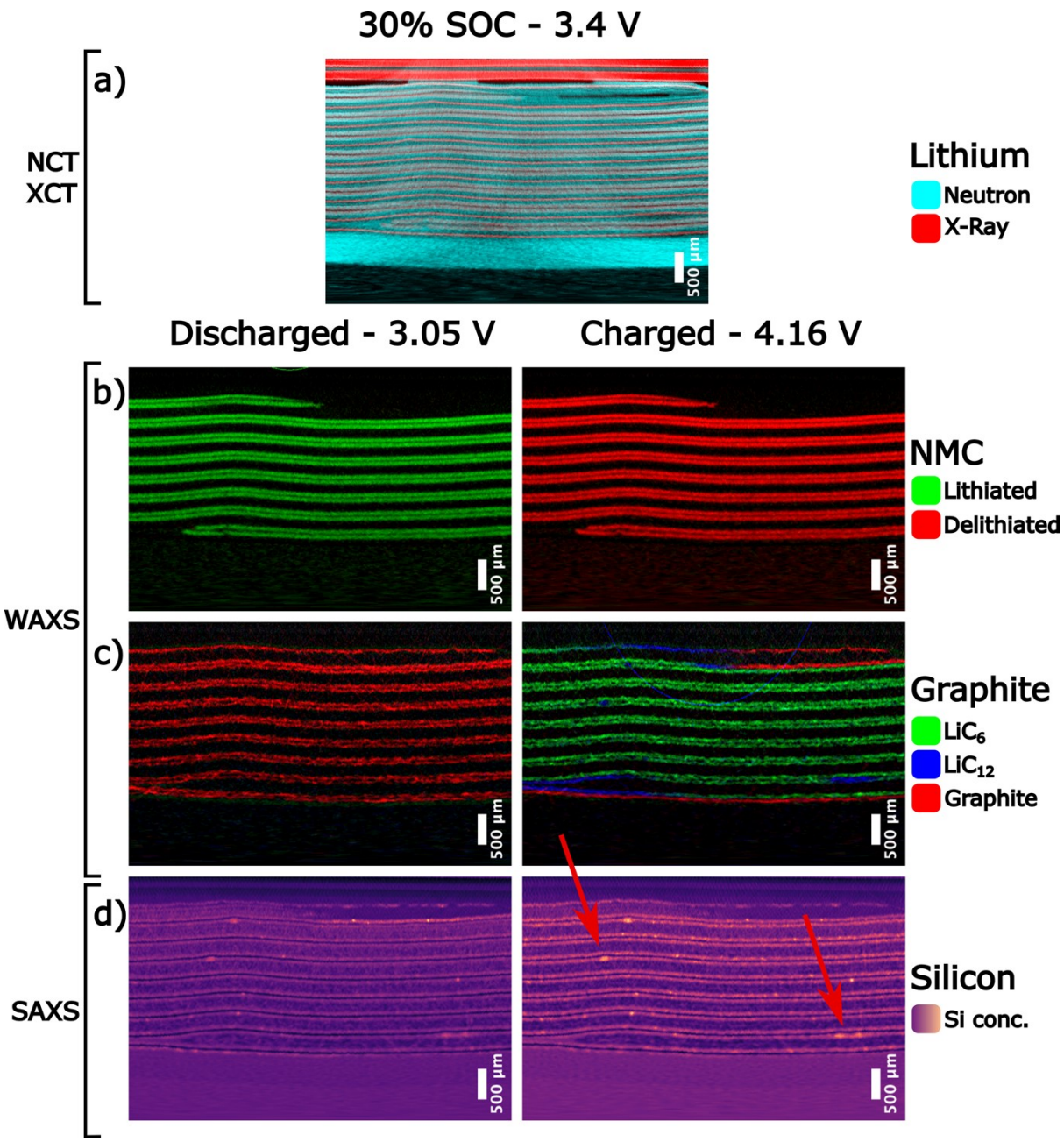

Figure S22: Virtually unrolled tomography slices of the fresh cell showing the same position in the same cell but obtained from the different imaging modalities. a) Color composite image showing the correlated NCT+XCT tomography measured at roughly 30% state of charge. b) Color composite image showing the distribution of lithiated NMC (green) and delithiated NMC (red). c) Color composite image showing the distribution of LiC_6 (green), LiC_{12} (blue) and graphite with partially lithiated phases (red). d) integrated SAXS intensity from q = 0.025 – 0.1 $Å^{-1}$, which correlates with concentrations of the nanostructured Si-composite.

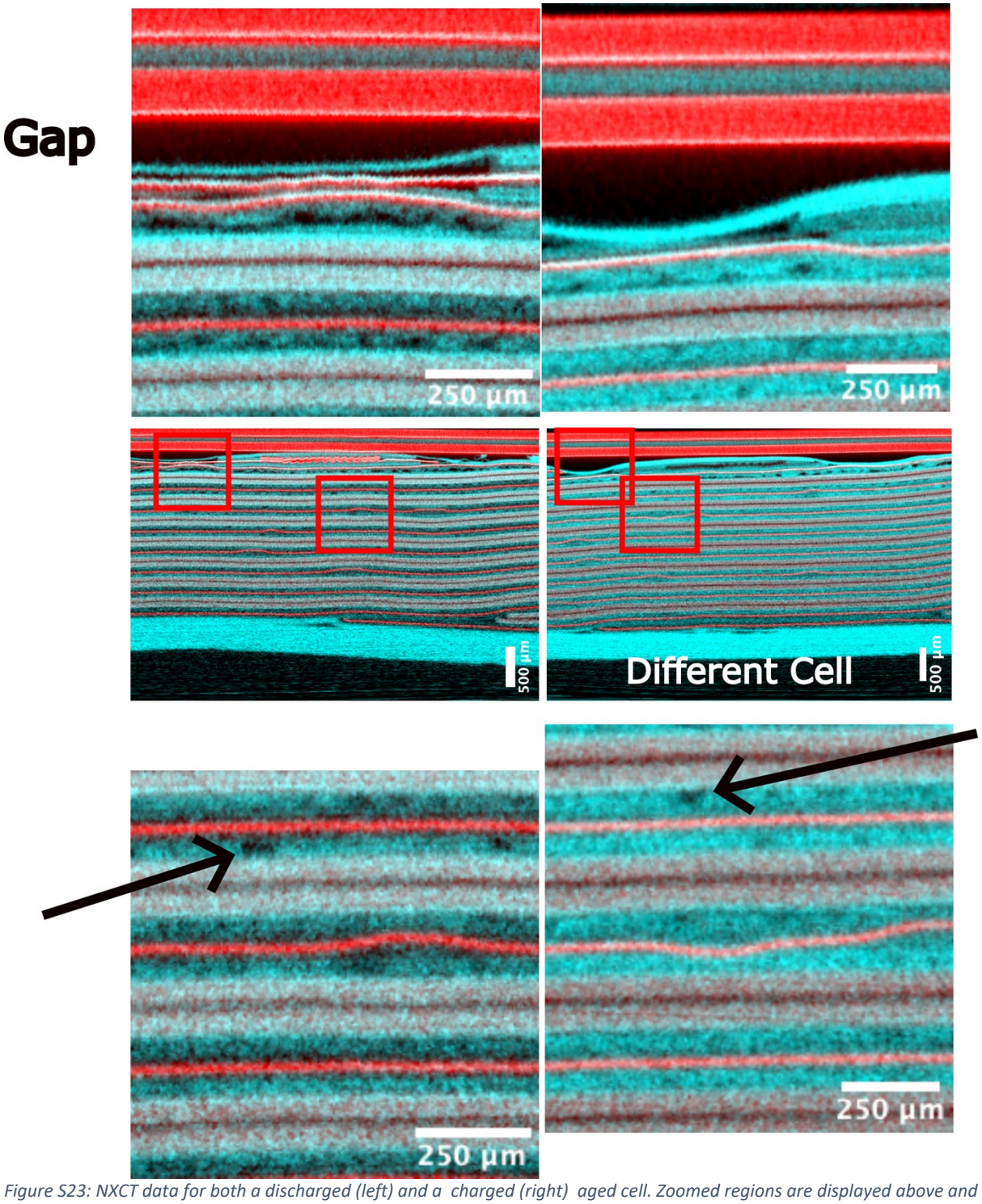

Figure S23: NXCT data for both a discharged (left) and a charged (right) aged cell. Zoomed regions are displayed above and below the images from Figure 2a). The relocation of lithium is immediately apparent, with the neutron intensity (cyan) shifting from the cathode to the anode Areas of lower intensity can be observed in both the discharged and charged state (black arrows).

Full Sized Unrolled Images

Due to size constraints cutouts were used for the main Fig. 2. The full figures are displayed in Figures S24 – S30.

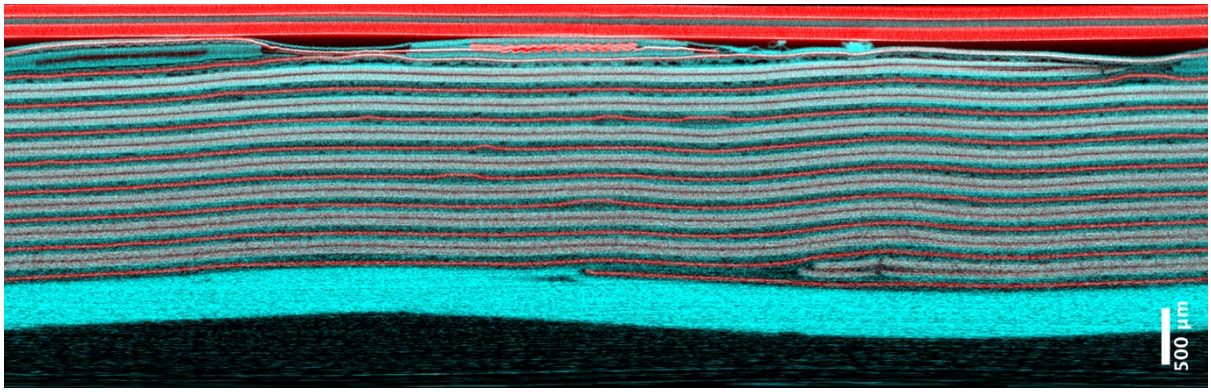

Figure S24: Unrolled NXCT image of the aged cell in the discharged state in full size. The unrolling preserved the dimension in the vertical direction (scale bar), but distorts the horizontal dimension from the polar transformation.

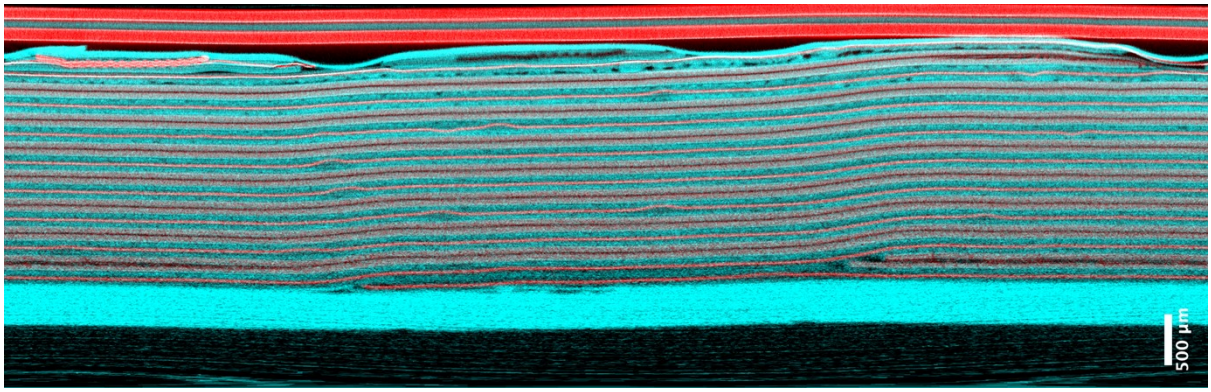

Figure S25: Unrolled NXCT image of an aged cell in the charged state in full size. The unrolling preserved the dimension in the vertical direction (scale bar), but distorts the horizontal dimension from the polar transformation. The depicted cell is different than the remaining images.

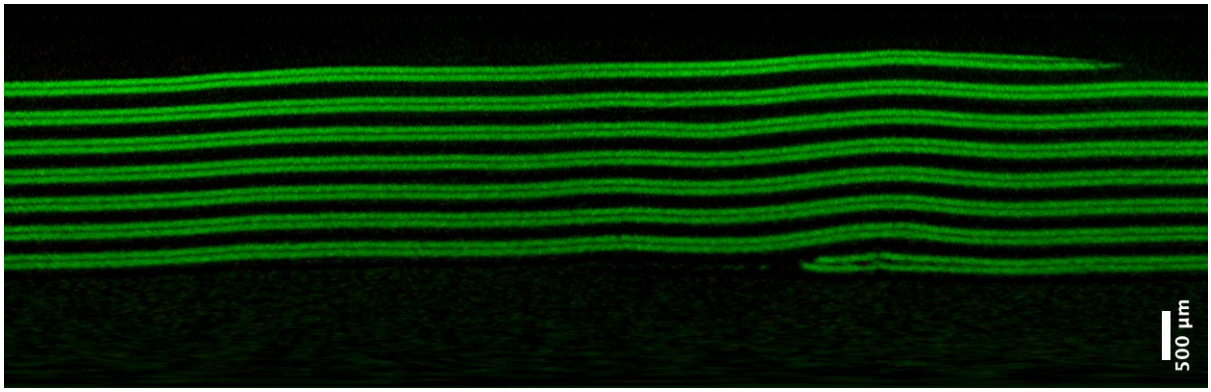

Figure S26: Unrolled composite image showing the distribution of lithiated NMC (green) and delithiated NMC (red) in the aged cell in the discharged state in full size. The unrolling preserved the dimension in the vertical direction (scale bar) but distorts the horizontal dimension from the polar transformation.

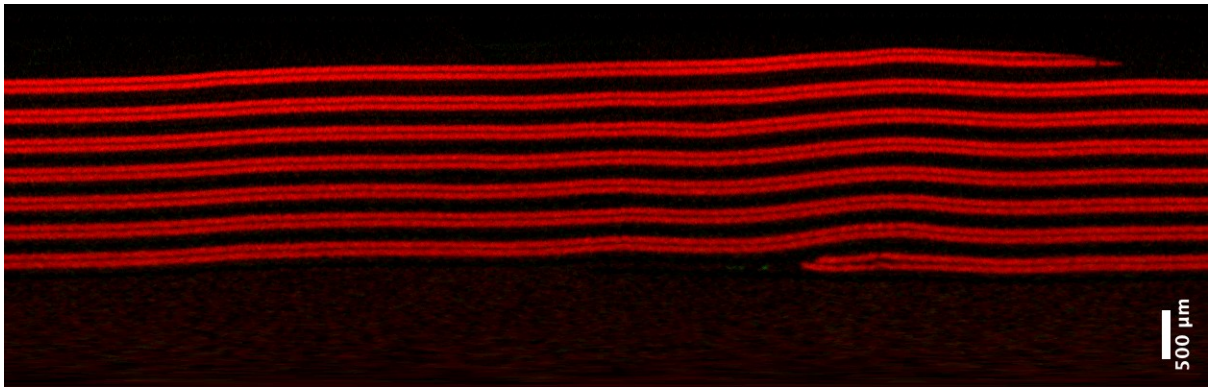

Figure S27: Unrolled composite image showing the distribution of lithiated NMC (green) and delithiated NMC (red) in the aged cell in the charged state in full size. The unrolling preserved the dimension in the vertical direction (scale bar) but distorts the horizontal dimension from the polar transformation.

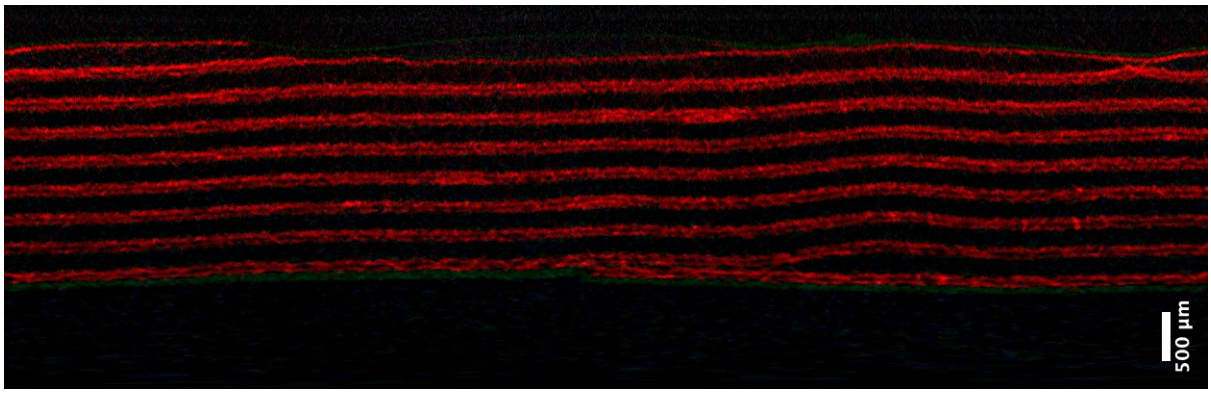

Figure S28: Unrolled composite image showing the distribution of LiC_6 (green), LiC_{12} (blue) and graphite with partially lithiated phases (red) in the discharged state in full size. The unrolling preserved the dimension in the vertical direction (scale bar) but distorts the horizontal dimension from the polar transformation.

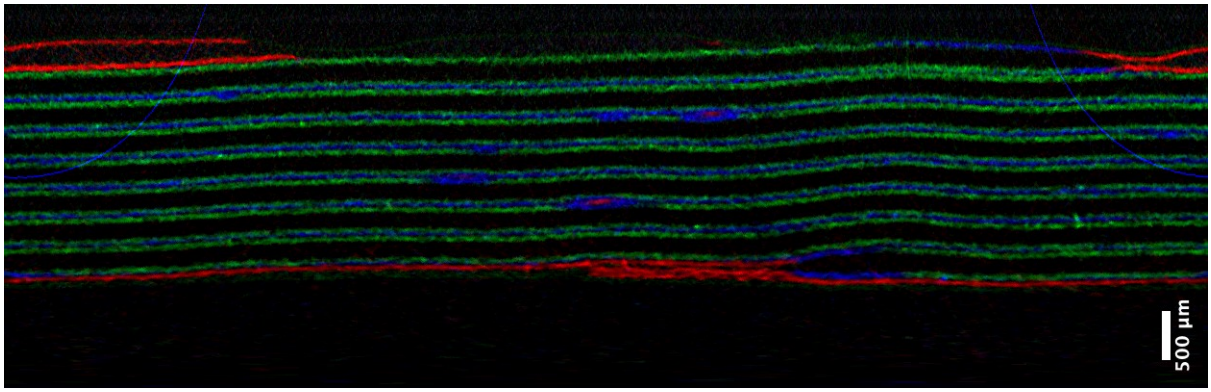

Figure S29: Unrolled composite image showing the distribution of LiC_6 (green), LiC_{12} (blue) and graphite with partially lithiated phases (red) in the charged state in full size. The unrolling preserved the dimension in the vertical direction (scale bar) but distorts the horizontal dimension from the polar transformation. A streak artifact stemming from the original reconstruction of the LiC_{12} phase is visible in the image as a blue arch. The shape is a result of the unrolling, which distorted the straight line. Poorly lithiated blue LiC_{12} domains are found spread around the cell, with some LiC_{12} patches containing unlithiated graphite centers.

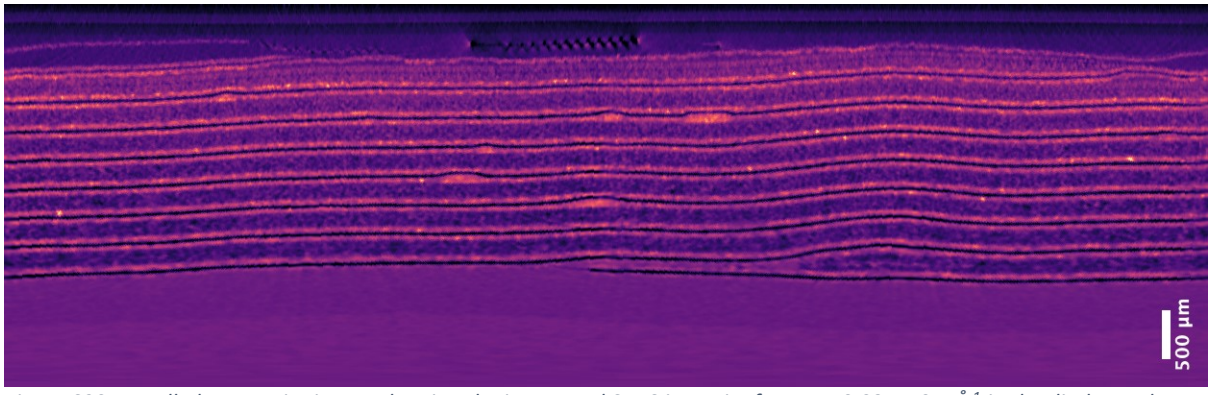

Figure S30: Unrolled composite image showing the integrated SAXS intensity from q = 0.025 – 0.1 Å^{-1} in the discharged state in full size. The unrolling preserved the dimension in the vertical direction (scale bar) but distorts the horizontal dimension from the polar transformation.

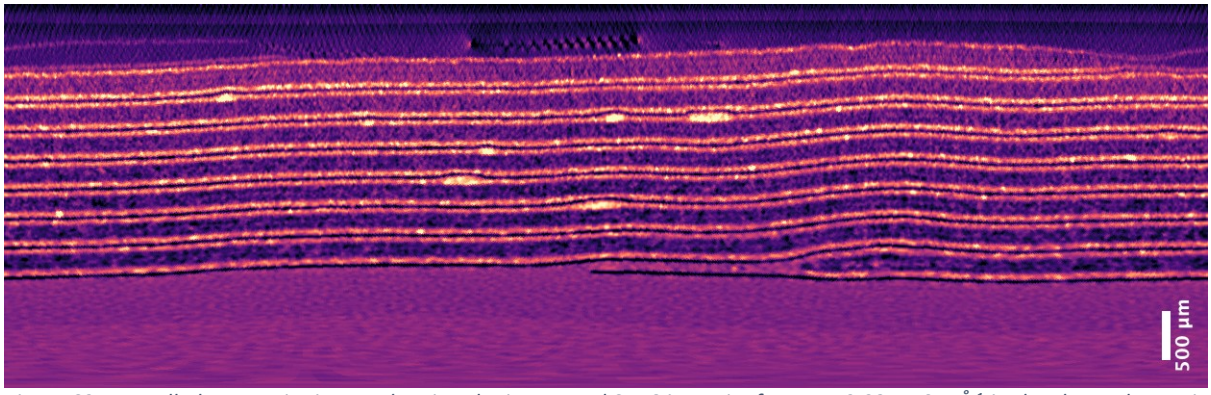

Figure S31: Unrolled composite image showing the integrated SAXS intensity from q = 0.025 – 0.1 Å^{-1} in the charged state in full size. The unrolling preserved the dimension in the vertical direction (scale bar) but distorts the horizontal dimension from the polar transformation.

Lithium Accumulations near Deformed Areas

Close to the deformed areas, lithium accumulations are visible in the NXCT scans. These are located close to the interface and are visible as a disk, which is broken in the areas of departure from the original position of the current collector, resulting in a circular shape. On the opposite and compressed side of the double layer, high lithiation can be observed as well, again in the shape of a ring which matches the bent area, as observed in S31. It is assumed that this feature developed as a consequence of the compression of the material due to the expansion of the silicon material on the other layer and subsequent deformation of the copper foil.

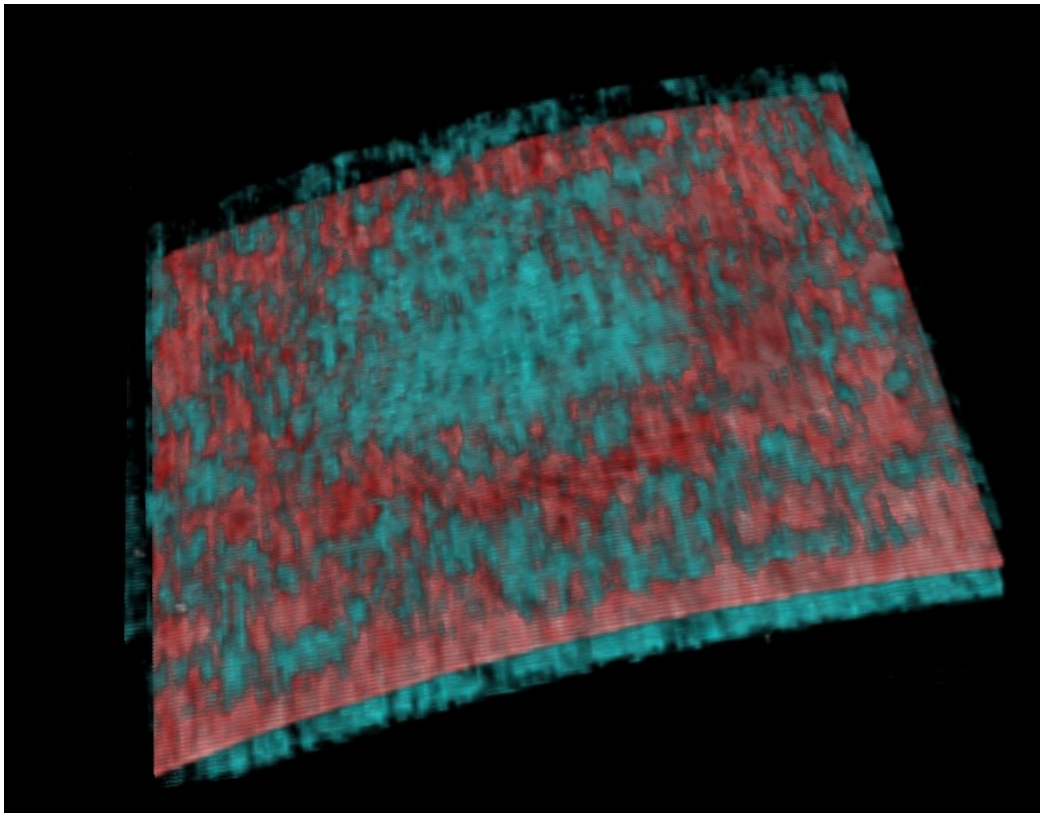

Figure S32: 3D rendering of a bent area in the discharged state showing a bend viewed from the opposite side, treated with color thresholding to highlight the current collector (red) and highly lithiated anode (cyan).

Internal characteristics of a macro scale defect in the fresh cell

As with main Figure 3 and S33, the images were unrolled and a cutout + profile taken of a deformed area. In this case, no graphite was found at the center of the deformed area, and instead only LiC_{12} is found.

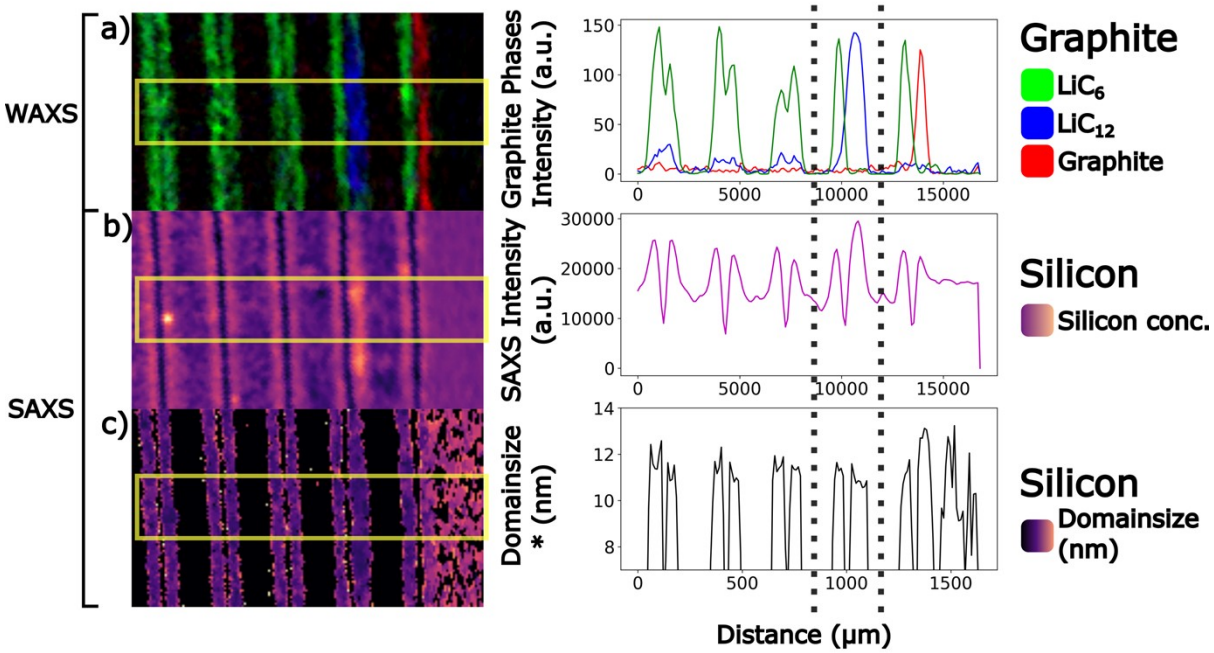

Figure S33: Internal characteristics of a macro-scale defect in the fresh cell. a) Composite image showing the distribution of LiC_6 (green), LiC_{12} (blue) and graphite plus partially lithiated phases (red). b) Integrated SAXS intensity, which correlates with concentrations of the nanostructured Si-domains. c) Calculated d, a characteristic value to describe the size distribution of the nanostructured Si-domains.*

Full Sized *Operando* Images

In the case of the *operando* scans the sinograms were constructed by stepwise combining 2 sets of interlaced scans together to minimize under-sampling artefacts while preserving some time resolution. As a result, the data is effectively averaged over a window of two interlaced scans, which took roughly 12 minutes per slice (for a total of 24 minutes) with a time difference between each frame of 12 minutes. Additionally, due to the relatively long scan time compared to the electrochemical reactions occurring, the bottom left, and top right quadrant show a slightly earlier point in time compared to the bottom right and top left quadrant. This effect is visible in Figure S34 where LiC_{12} appears to not be present at the start of the scan and only starts to appear during the already partially progressed acquisition, hence only being detected in some parts of the image.

Due to size constraints, only cutouts were used in the main Figure 5. The full images are displayed in Figures S34 – S42.

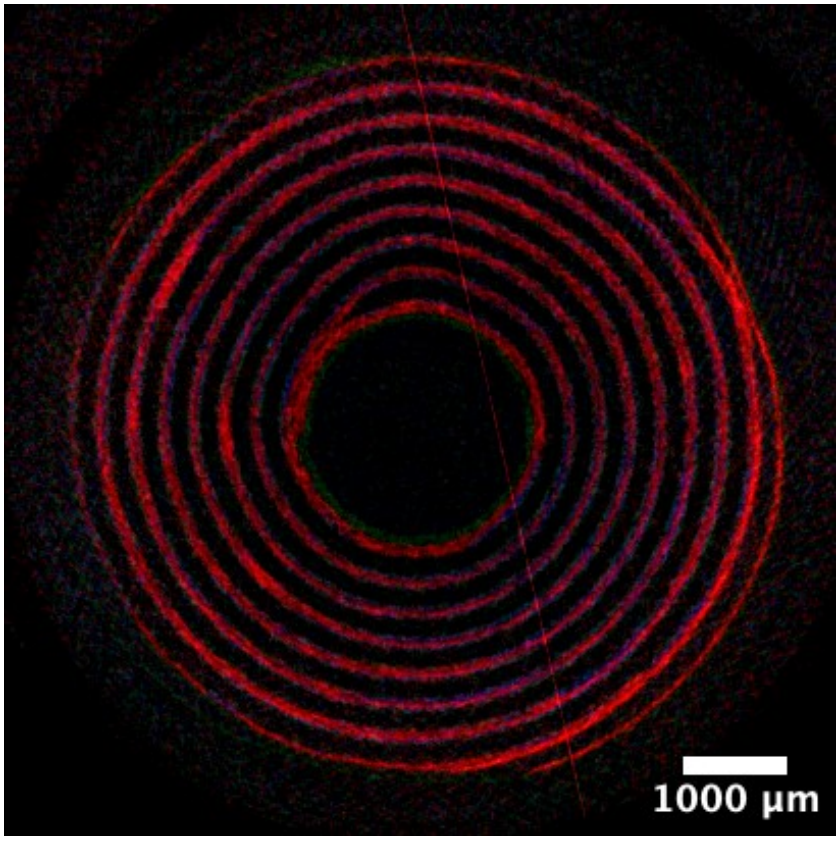

Figure S34: First full slice taken during the operando WAXS-CT measurement. Average over Q_{charge} 0 – 11.49 mAh → in total 5.74 mAh charged

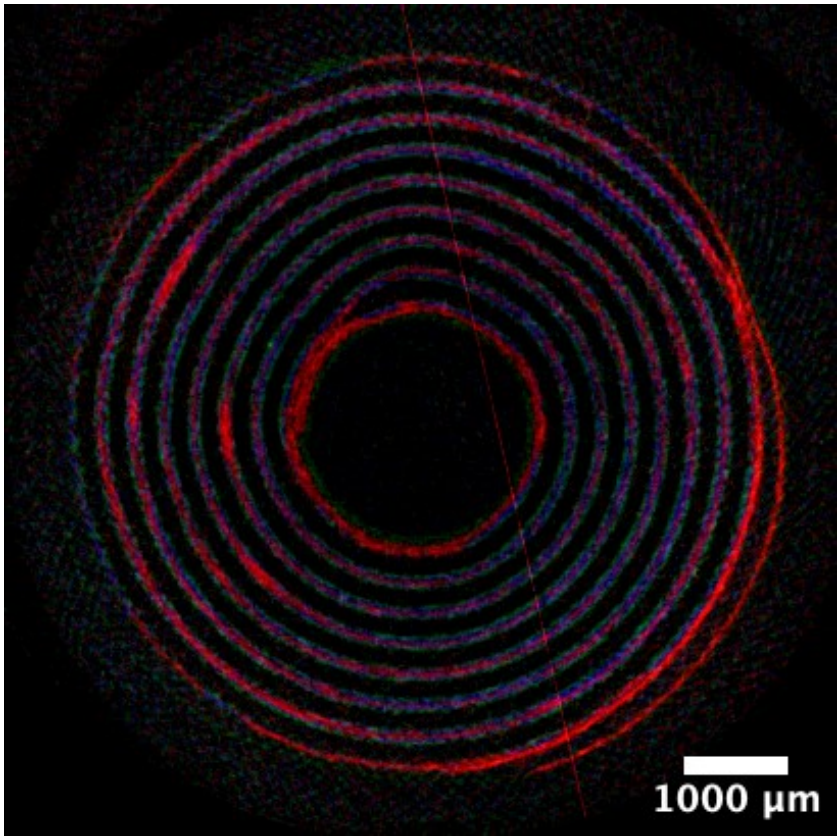

Figure S35: Second full slice taken during the operando WAXS-CT measurement. Average over Q_{charge} 6.08 – 15.36 mAh → in total 10.72 mAh charged.

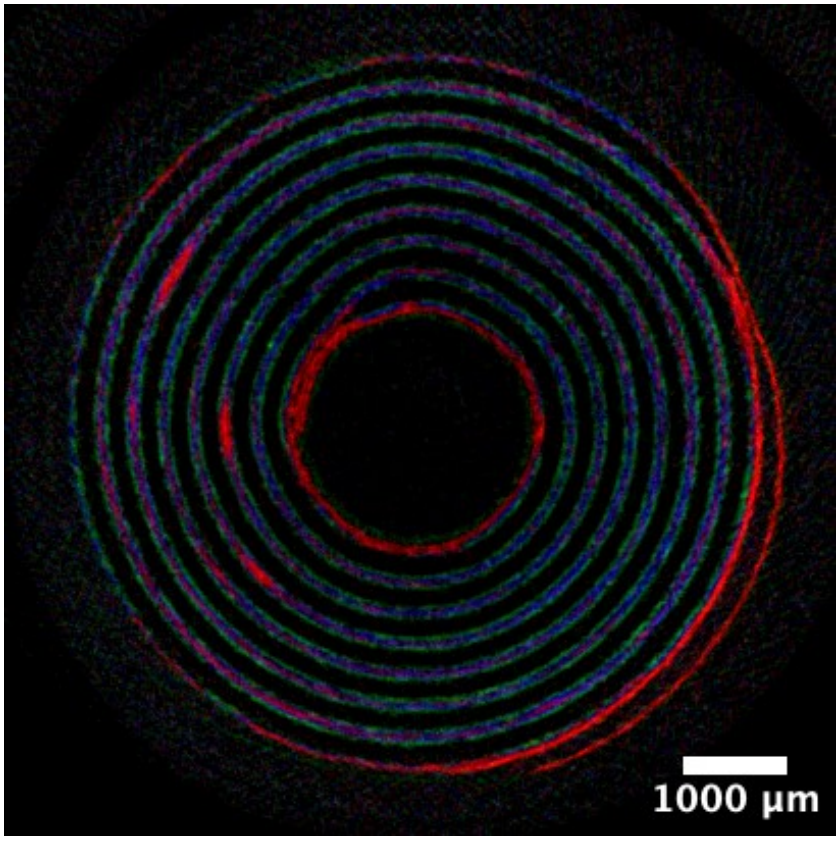

Figure S36: Third full slice taken during the operando WAXS-CT measurement. Average over Q_{charge} 11.49 – 18.14 mAh → in total 14.82 mAh charged.

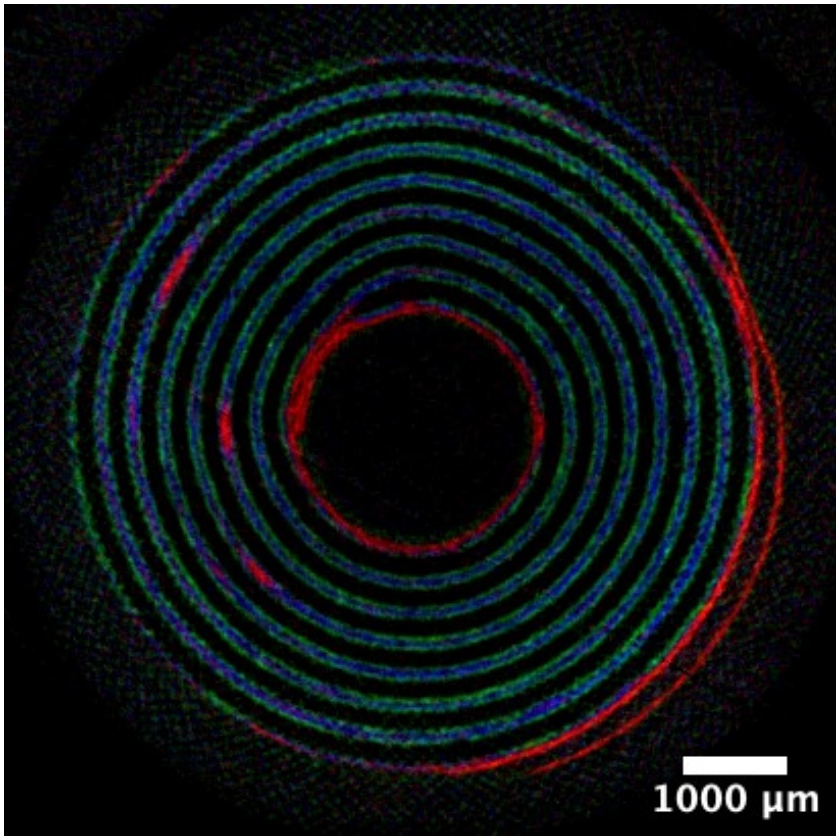

Figure S37: Fourth full slice taken during the operando WAXS-CT measurement. Average over Q_{charge} 15.36 – 20.28 mAh → in total 17.82 mAh charged.

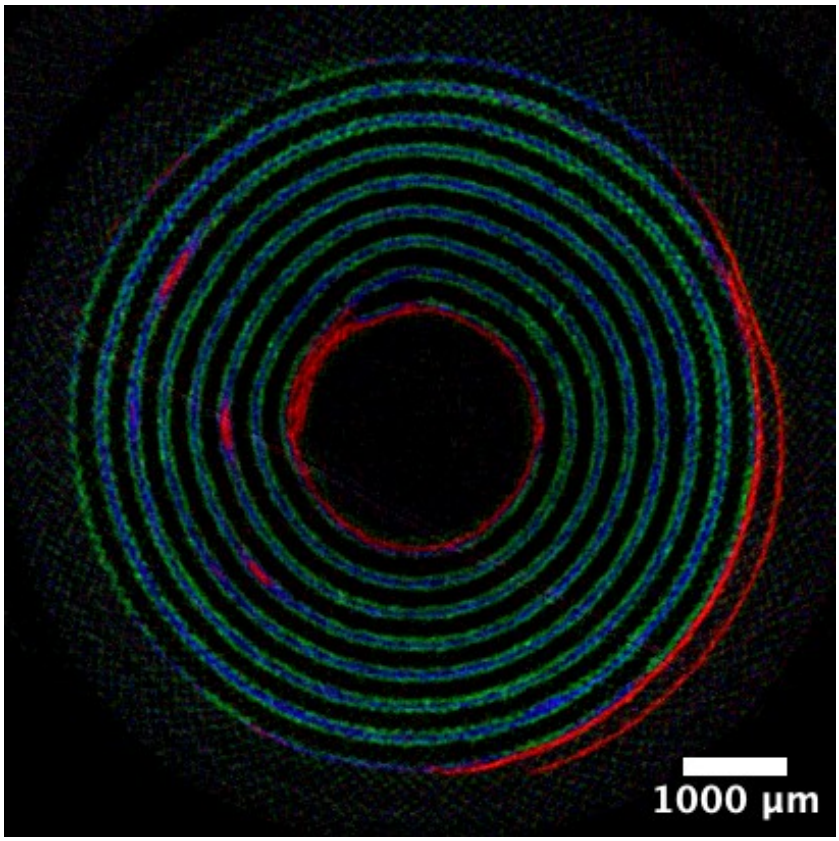

Figure S38: Fifth full slice taken during the operando WAXS-CT measurement. Average over Q_{charge} 18.14 – 22.21 mAh → in total 20.18 mAh charged.

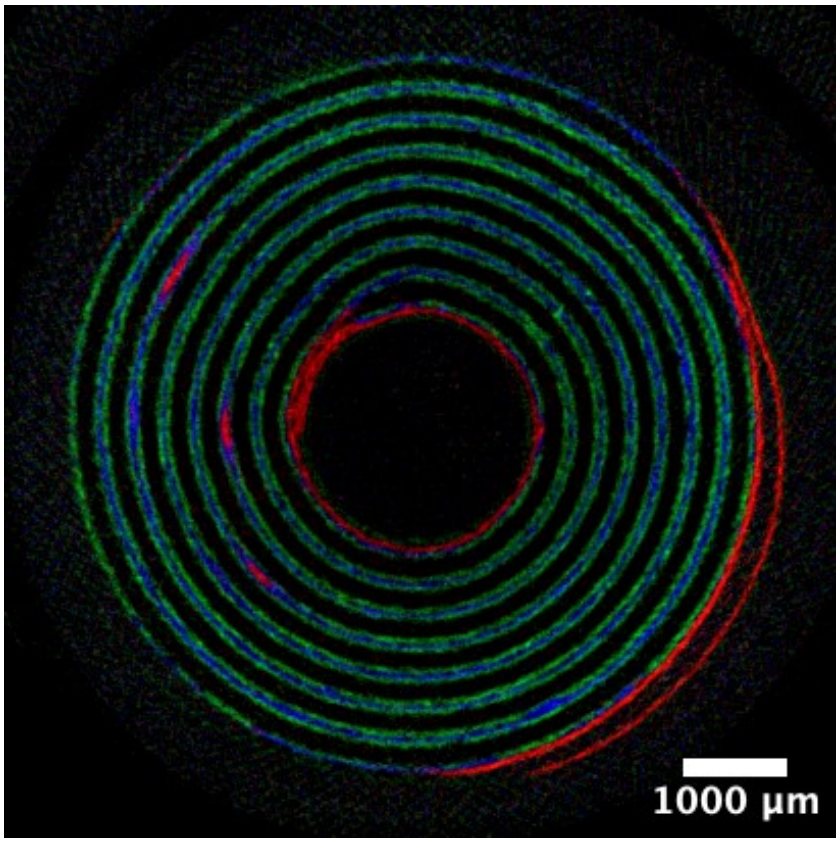

Figure S39: Sixth full slice taken during the operando WAXS-CT measurement. Average over Q_{charge} 20.28 – 23.93 mAh → in total 22.11 mAh charged.

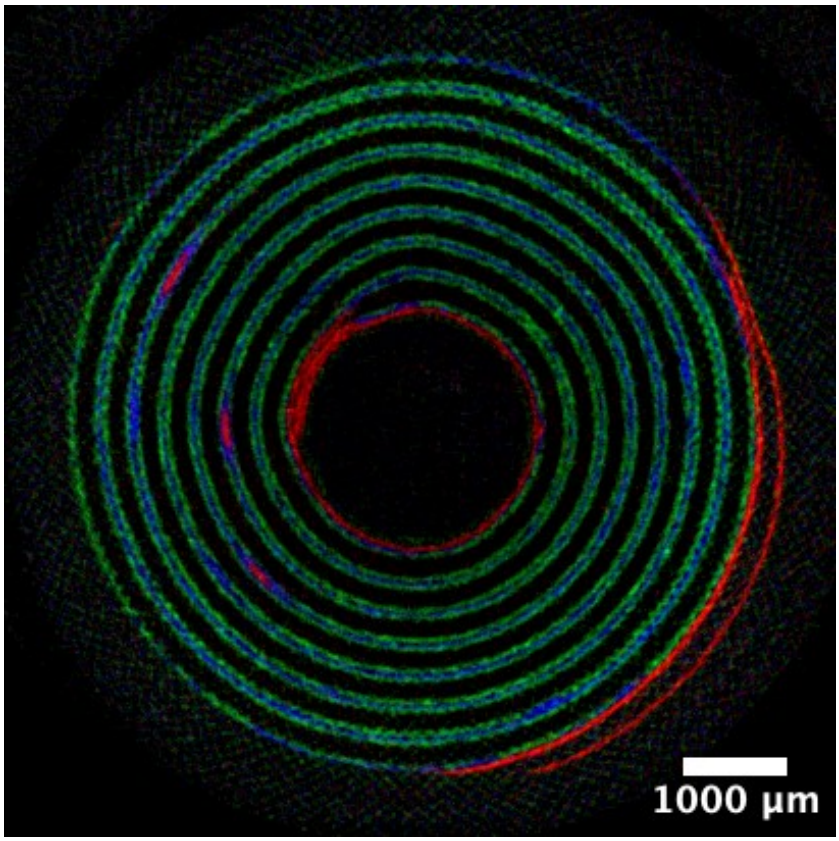

Figure S40: Seventh full slice taken during the operando WAXS-CT measurement. Average over Q_{charge} 22.21 – 25.59 mAh → in total 23.90 mAh charged.

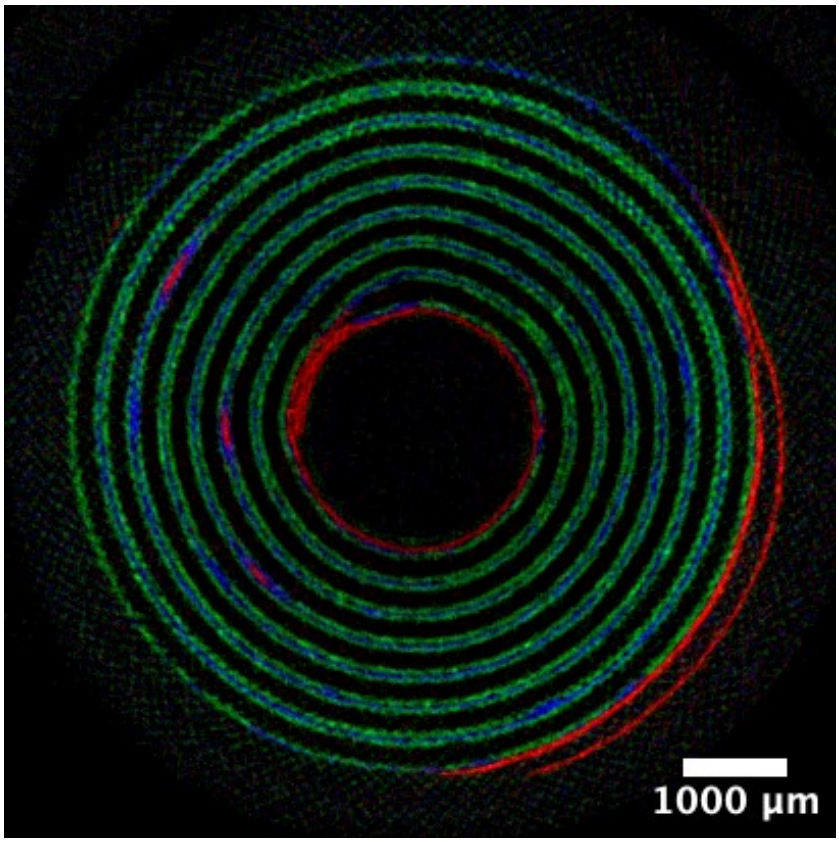

Figure S41: Eight full slice taken during the operando WAXS-CT measurement. Average over Q_{charge} 23.93 – 27.28 mAh → in total 25.61 mAh charged.

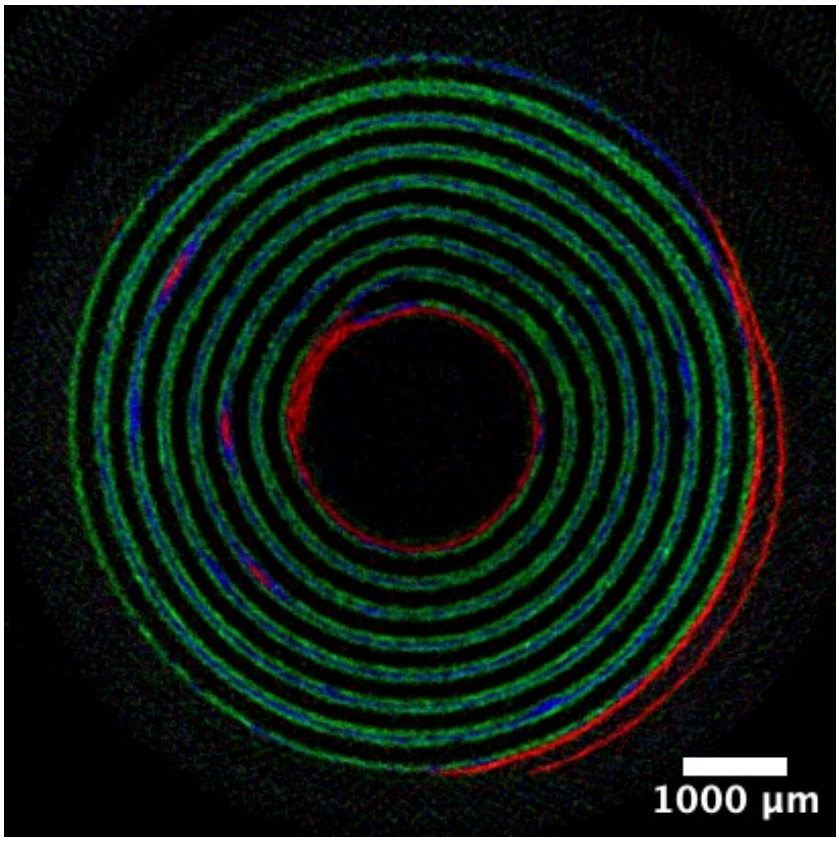

Figure S42: Ninth full slice taken during the operando WAXS-CT measurement. Average over Q_{charge} 25.59 – 28.54 mAh → in total 27.07 mAh charged.

Electrochemistry

The electrochemistry was applied to the cells using a BioLogic SP-300 potentiostat. The fresh cell was first charged from the as delivered state by applying a 1C current. This was followed by a constant voltage step where the cell was held at 4.2 V and allowed to relax for 30 minutes for the voltage to stabilize before SWAXS-CT measurements were started. The discharge followed the same protocol, but the cell was instead held at 2.8 V. Figure S43 shows the electrochemical data for the fresh cell.

The aged cell was charged with the same settings as the fresh cell during the experiment. Due to a user error, the cell was accidentally discharged for a short time and had to be recharged before the actual data was measured. Figure S44 shows the electrochemistry data for the aged cell, with the accidental discharge visible. It should be noted that while the cell was charged to and held at 4.2V, it immediately self-discharged once the current was removed. This behavior was also observed with other cells of this series that were aged in a similar fashion (not shown).

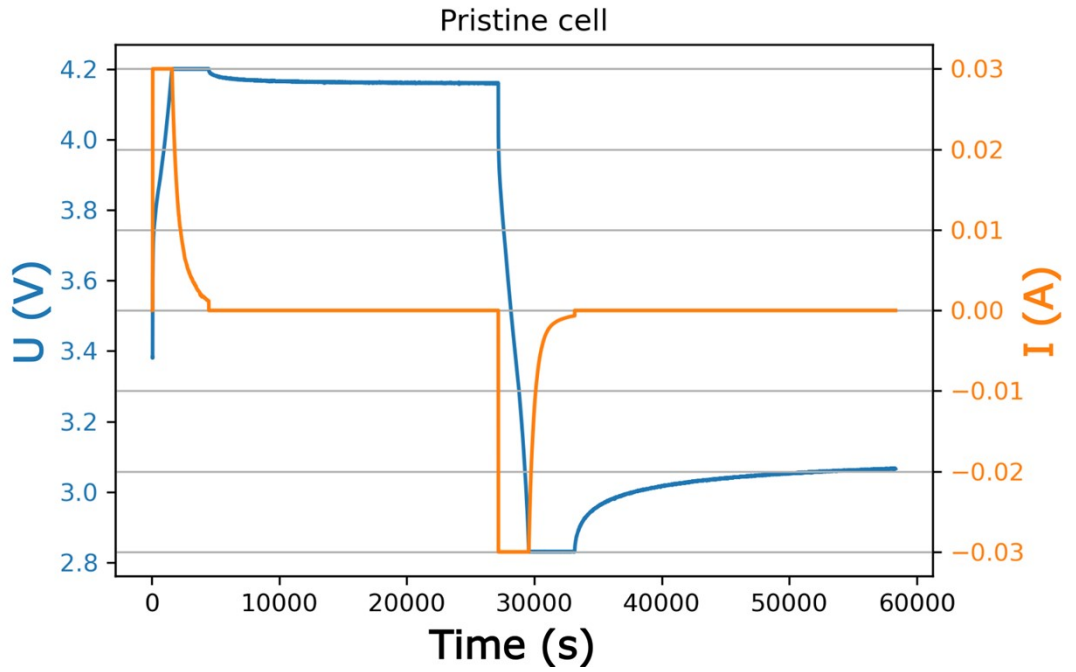

Figure S43: Electrochemical cycle performed with the fresh cell during the SWAXS-CT measurements.

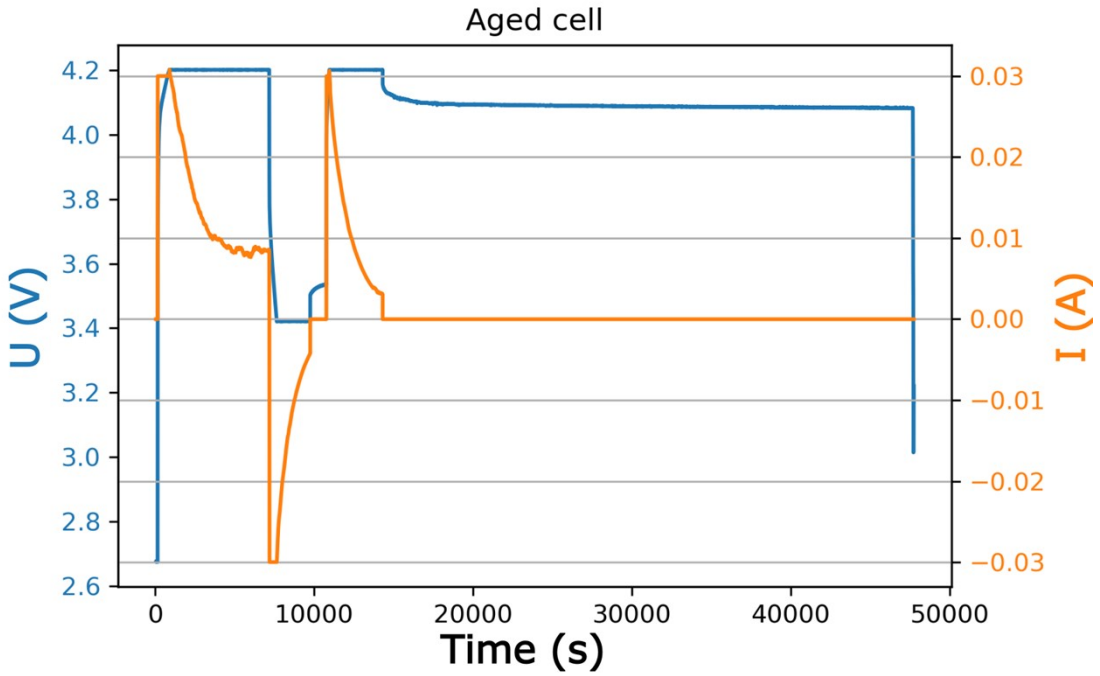

Figure S44: Electrochemical cycle performed with the aged cell during the SWAXS-CT measurements. Due to a user error the cell was accidentally discharged for a short time. This was corrected by restarting the charging program.

Integration Ranges

To evaluate the X-Ray Diffraction data contained in the WAXS-CT scans every diffractogram is integrated in the peak ranges given in Main Text Table 1. Figure S45 shows the sum of all X-Ray diffraction patterns for the charged and discharged aged cell. By selecting appropriate integration regions images highlighting certain crystallographic phases are then generated (e.g. S17-S21) and combined in false color to highlight heterogeneities (e.g. S34-S42).

Studies focusing on the NMC tend to investigate the 003 Bragg reflection. However, due to the hard X-rays used in this experiment, the 003 reflections in the lithiated vs delithiated form are not well separated and have significant overlap. Instead, the better separated 113 and 110 reflections are used to map lithiated vs delithiated NMC.

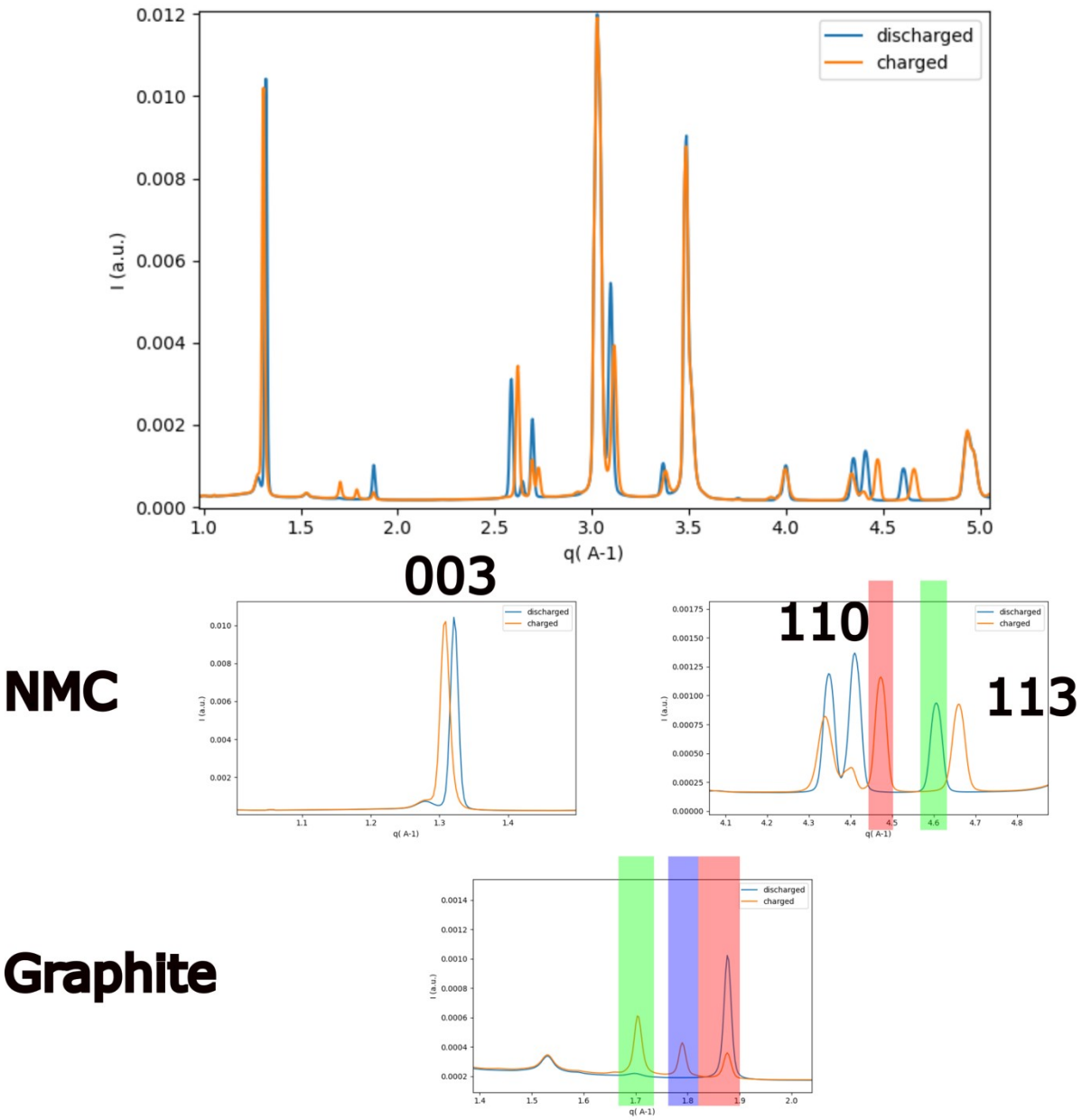

Figure S45: Cutout of the sum of all XRD-Patterns for the aged cell in the discharged vs charged state. Colored boxes represent the integration range as well as corresponding color used in the false color images. The separation between the different graphite phases can be observed at the bottom.

d* determination

Raw 1D SAXS data (Figure S46) are evaluated by a fitting procedure (Figure S47) to extract a metric labeled d* that relates to the nanoscale size of the silicon domains at a given state of lithiation.

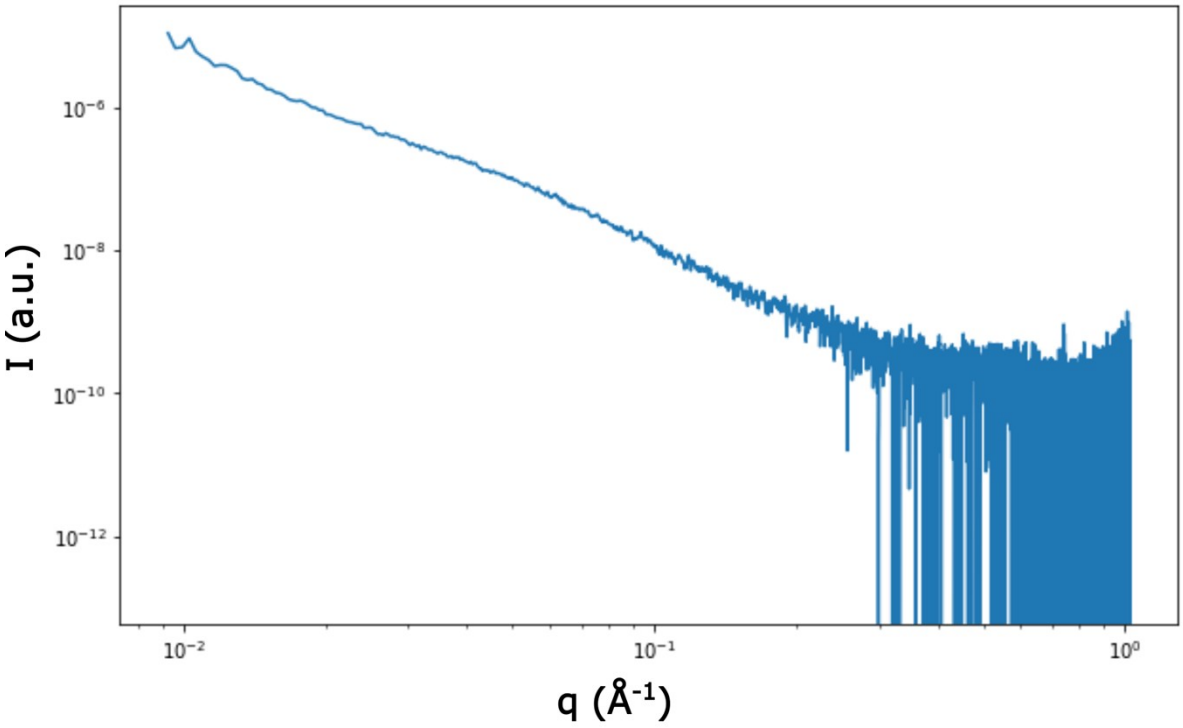

Figure S46: Raw 1D SAXS data displayed in a log-log plot.

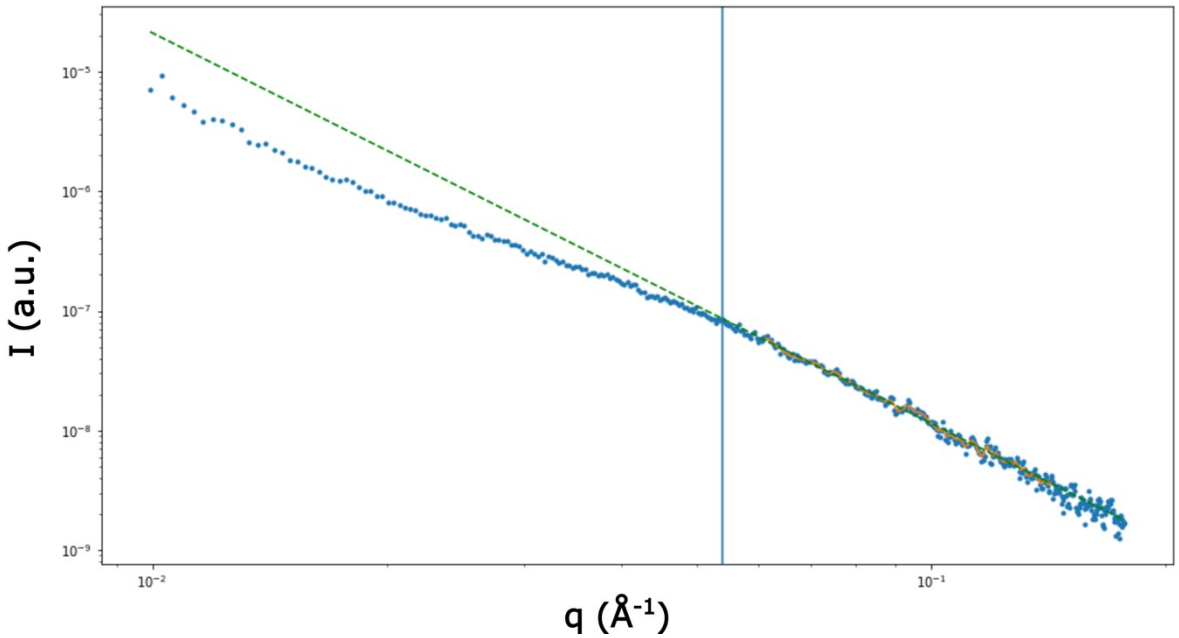

Figure S47: Exemplary d evaluation. A q^{-x} fit (green) was performed in the bottom 70 - 20% of 1D SAXS profile datapoints (orange line). The q* value is determined at the departure point and marked with a vertical line (here, 0.053 $Å^{-1}$). The metric d* is defined as $d^*=2\pi/q^*$ and corresponds to a size where the signal is not only arising from interfaces, therefore indicating a range for typical domain size (11.8 nm here).*

The decaying intensity observed in the SAXS data arises from scattering from the different components in the anodes: large graphite particles, composite silicon phase composed of $FeSi_2$ particles embedded into a continuous nanostructured amorphous silicon matrix, carbon black particles and binder. It evolves depending on the lithiation degree of silicon, Li_xSi, both in intensity and shape, passing from an unshaped simple decaying q^{-a} law (x=0) to a more complex profile, where an excess intensity grows at high q (up to x > 3 typically). It is difficult to quantitatively model these effects using a two-phase model formalism, e.g. expressing the I(q) as the product of volume, contrast term, form and structure factors(7,11), because there are more than two-phases potentially in contact with silicon: graphite in different lithiation states Li_xC_6, binder, $FeSi_2$ particles, and a thick SEI which is chemically evolving and dynamically reforming in the system during the cycling.(12,13) In a previous work(7), we evaluated the growing of silicon nanodomains during lithium uptake by introducing a simple, model-independent metric, determined as $d^*=2\pi/q^*$, where q* is a typical value where an inflexion appears in the I(q) profiles, that is the signature of silicon expansion.

In this previous publication(7), it was possible to subtract the initial SAXS data from *operando* profiles, and better highlight the changes using the differential intensity profiles. A clear low-q slope and a high-q slope could be defined in these curves, where intercept was related to some typical size within the silicon domains. This corresponds to the intermediate zone between Porod's behavior (particles interfaces with their surrounding medium, at high q) and the beginning of a Guinier-type region corresponding to the object dimensionality and shape (low-q). This method is approximate, but useful to compare different states of the same cell. In the 2-dimensional data of this study such a SAXS profile exists for each voxel, but subtracting the data in the discharged state introduces errors and noise. This is due to some significant deviations in the local concentrations and expansions plus deformations occurring inside the cell. Therefore, we worked on the raw data, free from any manipulations except by the reconstruction algorithm and radial integration.

A sample of this raw data is shown in Figure S48 for the formed (fresh) cell and the aged cell, both in charged and discharged states, and extracted from specific locations as indicated in the corresponding side images. To further highlight the differing behaviour of bent areas, agglomerates and normal parts the curves were replotted in figure S49 to enable a direct comparison within states of charge and health. We can observe that data taken in « regular » regions of the formed cell (top line) are very stable across the anode depth, with profiles highly reproducible from one location to another. The profiles are also similar to what was reported on this material in our previous paper(7). Clearly, in the delithiated state, there is only one decaying slope. The fact that this curve is unshaped can have different origins, with one explanation being a lack of sufficient contrast between Si and $FeSi_2$ in the fully delithiated state. However, it is also possible that the structure before lithiation and ageing is disorganized to the point that no domains are clearly defined. These explanations also do not contradict each other, making it possible that both effects are responsible. Note that the mean delithiated I(q) obtained by averaging the four positions reproduced in Figure S48 is kept as a red dashed line in all the other positions, for comparison. This is also done for the lithiated profile (dashed blue line), where we can see the curvature in the shape because of the growing of lithiated silicon nanoscale domains. A d* value is easily obtained using departure from the high-q slope, as indicated in the figure by an arrow. It falls in the range of 12 nm (Table S1), as previously seen in (7). If we consider the regular location in the aged cell

now, we can see that 1) the data is also very stable across different locations, although there is a bit more dispersion with respect to the fresh cell, probably as an effect of aging; 2) the delithiated state is still represented by a unique decaying slope over the full q-range, therefore indicating full extraction of all lithium ions in some regions of the cell, even after 700 cycles. Interestingly, however, we notice that the d* obtained from the lithiated data has increased to 14 nm, with a higher spread of the SAXS intensity values as compared to fresh cell. This tells us that the aged cell does not behave as the fresh one, and the morphology of the silicon phase has changed, but the (de)lithiation process seems to be mostly maintained.

In contrast, the situation is completely different in the bent regions. The formation cycles yield some degree of swelling during the charge (d* = 11 nm, Table S1), but the discharge is irreversible, and the defective regions are clearly kept in a lithiated state and d* stays around 11 nm, even after ageing the cell. It is likely that the region has expanded dramatically, got disconnected, and ions could not be removed on discharge from the Li_xSi regions. The agglomerates observed also behave similar to the bent regions. Swelling seems to occur during the charge and d* rises to around 11 nm as well. However, once the cell is discharged the d* seems to rise to almost 12 nm, contrary to the expected behavior. This can be explained if one considers that parts of the agglomerates still show some activity. If parts of the agglomerates are still connected and charge/discharge semi-normally these areas would not contribute to the q-range probed in the d* analysis once the cell is discharged, as observed with the normal areas in the fresh cell. This leaves only the areas “stuck” in the expanded state to be probed with the d* in the discharged state, resulting in a higher value than observed in the charged state. Indeed, the d* of 11.6 nm matches closely with the value observed in the areas of the fresh cell behaving normally. Further, some agglomerates seem to almost fully discharge/charge, implying more complex conditions for this defect type.
This phenomenon then implies that after long-term cycling the defects are regions that are mostly inactive, showing very similar SAXS data as in the formed cell. Hence, the damage is produced right after the first lithiation, and the material in large agglomerates is mostly disconnected, therefore not contributing to the capacity of the cell, with the smaller agglomerates still showing slightly more activity.

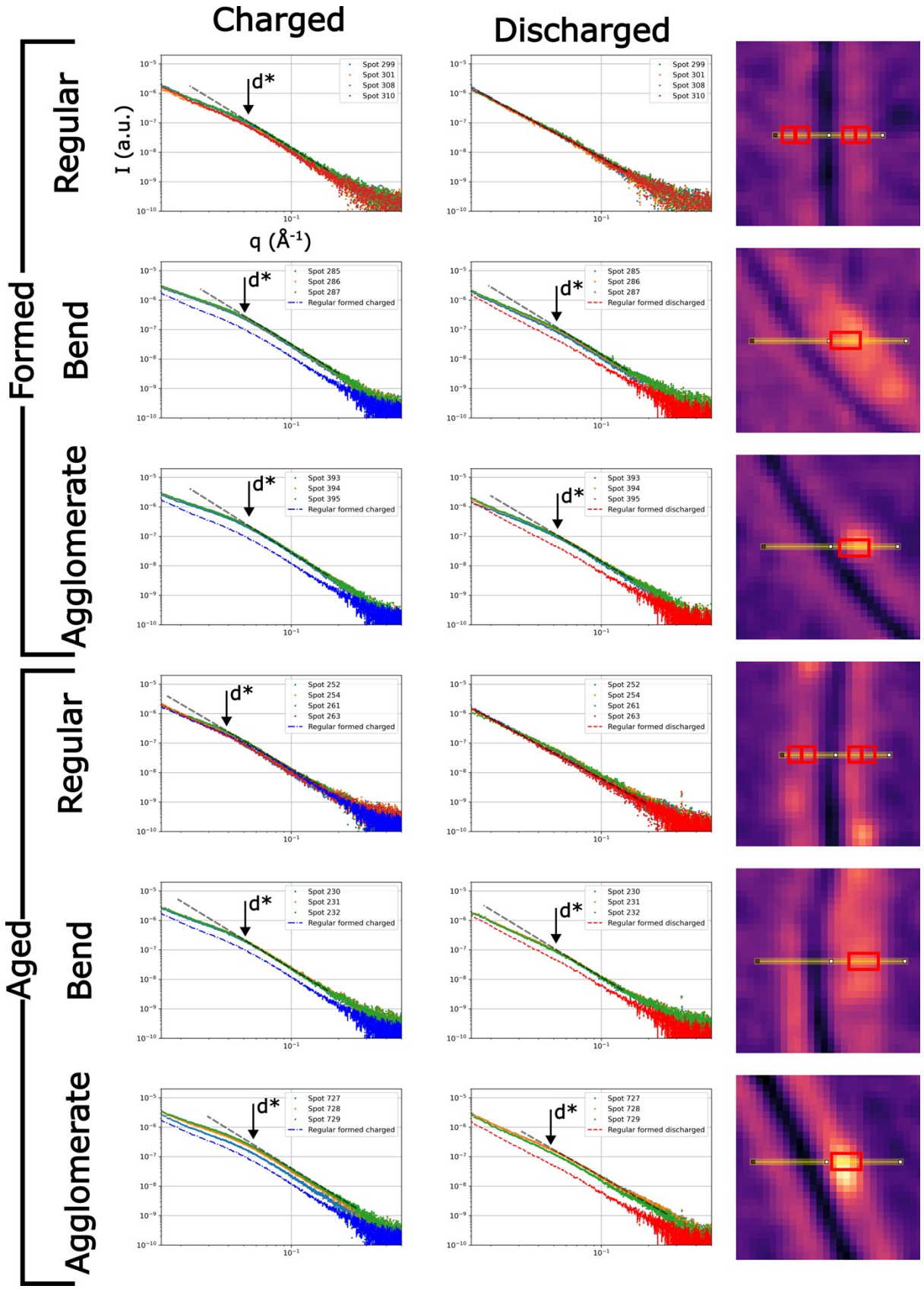

Figure S48: Exemplary raw SAXS profiles extracted in regular, bent and agglomerate areas for both the formed and aged cell. The charged state is depicted on the right and the discharged state om the left, with a reference line to show the reference state in regular areas of the fresh cell.

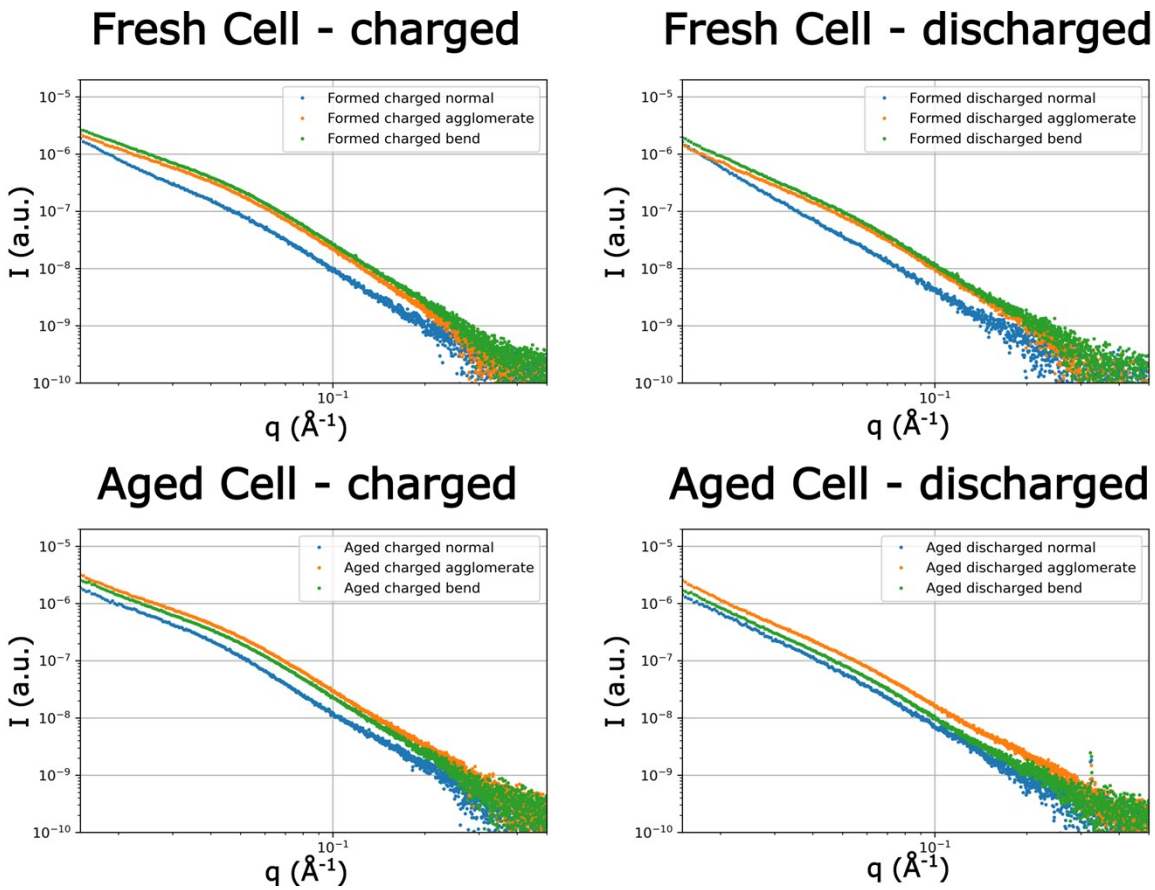

Figure S49: Averaged raw SAXS profiles extracted in regular, bent and agglomerate areas for both the formed and aged cell plotted against each other to highlight the differences between the defect within a certain state of health/charge.

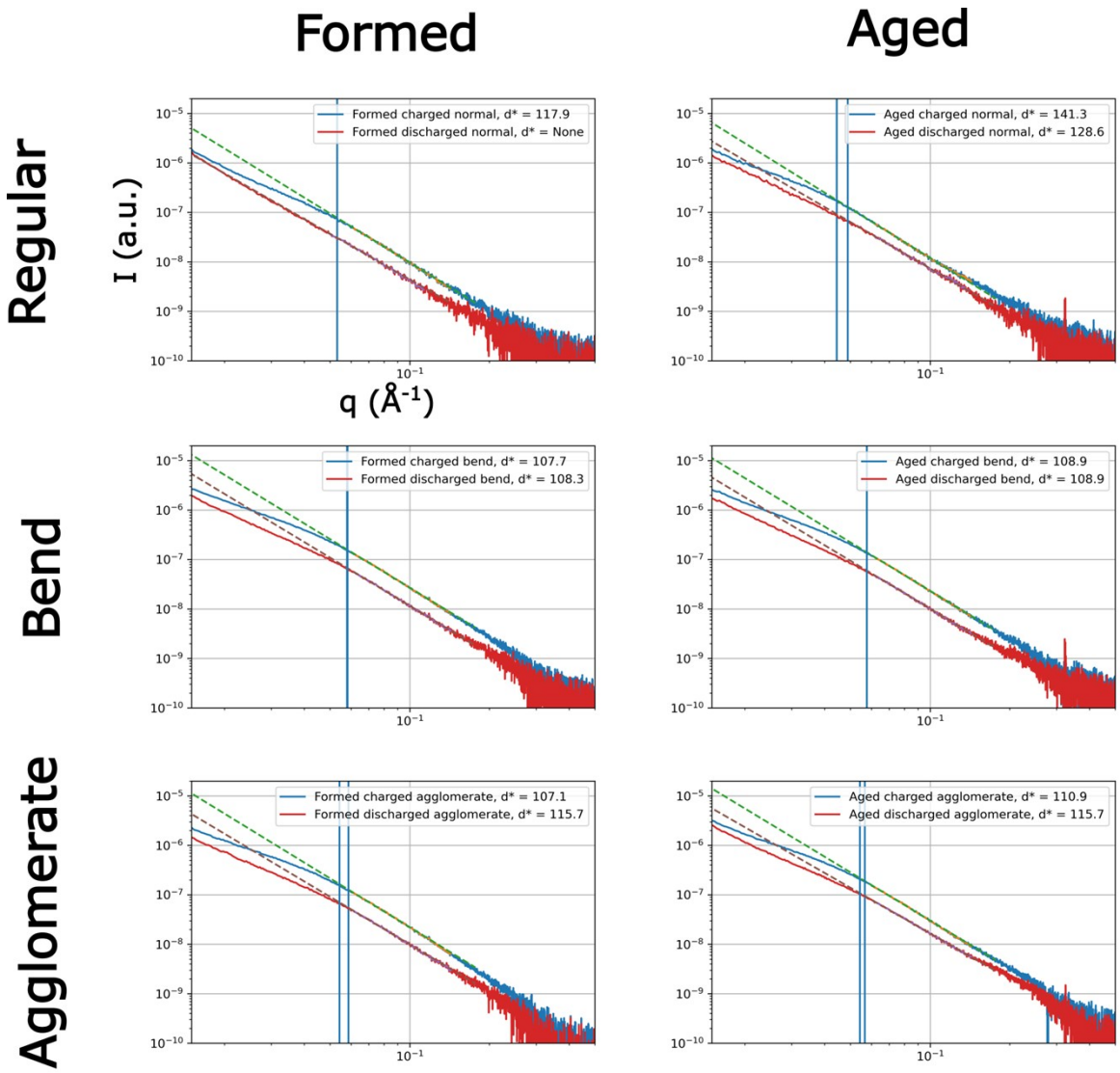

Figure S50: Averaged raw SAXS profiles extracted in regular, bent and agglomerate areas for both the formed and aged cell plotted against each other to highlight the differences between the discharged and charged state for the different types. The output d is in Å.*

Table S1: Representative d values extracted from the averaged data shown in S48 and S49.*

	Normal	Bend	Agglomerate
Fresh - charged	11.8 nm	10.8 nm	10.9 nm
Fresh - discharged	None	10.8 nm	11.6 nm
Aged - charged	14.1 nm	10.9 nm	11.1 nm
Aged - discharged	12.9 nm	10.9 nm	11.6nm

References

1. Tengattini A, Lenoir N, Andò E, Giroud B, Atkins D, Beaucour J, et al. NeXT-Grenoble, the Neutron and X-ray tomograph in Grenoble. Nucl Instrum Methods Phys Res Sect Accel Spectrometers Detect Assoc Equip. 2020 Jul;968:163939.

2. Vogelgesang M, Farago T, Morgeneyer TF, Helfen L, dos Santos Rolo T, Myagotin A, et al. Real-time image-content-based beamline control for smart 4D X-ray imaging. J Synchrotron Radiat. 2016 Sep 1;23(5):1254–63.

3. Faragó T, Gasilov S, Emslie I, Zuber M, Helfen L, Vogelgesang M, et al. *Tofu* : a fast, versatile and user-friendly image processing toolkit for computed tomography. J Synchrotron Radiat. 2022 May 1;29(3):916–27.

4. Tudisco E, Jailin C, Mendoza A, Tengattini A, Andò E, Hall SA, et al. An extension of digital volume correlation for multimodality image registration. Meas Sci Technol. 2017 Sep 1;28(9):095401.

5. Stamati O, Andò E, Roubin E, Cailletaud R, Wiebicke M, Pinzon G, et al. spam: Software for Practical Analysis of Materials. J Open Source Softw. 2020 Jul 13;5(51):2286.

6. Dianoux AJ, Institut Laue-Langevin, editors. Neutron data booklet. 2. ed. Philadelphia, PA: Old City; 2003.

7. Berhaut CL, Dominguez DZ, Kumar P, Jouneau PH, Porcher W, Aradilla D, et al. Multiscale Multiphase Lithiation and Delithiation Mechanisms in a Composite Electrode Unraveled by Simultaneous *Operando* Small-Angle and Wide-Angle X-Ray Scattering. ACS Nano. 2019 Oct 22;13(10):11538–51.

8. Kieffer J, Karkoulis D. PyFAI, a versatile library for azimuthal regrouping. J Phys Conf Ser. 2013 Mar 22;425(20):202012.

9. Van Aarle W, Palenstijn WJ, De Beenhouwer J, Altantzis T, Bals S, Batenburg KJ, et al. The ASTRA Toolbox: A platform for advanced algorithm development in electron tomography. Ultramicroscopy. 2015 Oct;157:35–47.

10. Van Aarle W, Palenstijn WJ, Cant J, Janssens E, Bleichrodt F, Dabravolski A, et al. Fast and flexible X-ray tomography using the ASTRA toolbox. Opt Express. 2016 Oct 31;24(22):25129.

11. Hamley IW. Small-angle scattering: theory, instrumentation, data, and applications. Hoboken, NJ, USA Chichester, West Sussex, UK: Wiley; 2021. 278 p.

12. Kumar P, Berhaut CL, Zapata Dominguez D, De Vito E, Tardif S, Pouget S, et al. Nano-Architectured Composite Anode Enabling Long-Term Cycling Stability for High-Capacity Lithium-Ion Batteries. Small. 2020 Mar;16(11):1906812.

13. Vorauer T, Kumar P, Berhaut CL, Chamasemani FF, Jouneau PH, Aradilla D, et al. Multi-scale quantification and modeling of aged nanostructured silicon-based composite anodes. Commun Chem. 2020 Dec;3(1):141.